HEMODYNAMIC MONITORING: FROM MRI TO BEDSIDE

by

KEVIN JAMES WU

(Under the Direction of TSZ HO TSE)

ABSTRACT

Magnetohydrodynamic voltages (V_{MHD}), induced from the interaction between blood flow and an external magnetic field, have been shown to be a useful physiological monitoring metric. V_{MHD} was first observed in intra-MRI ECGs and can be a predictor of blood flow. An adaptive filtering method was developed to try and obtain better ECG_{Real} by utilizing an isolated V_{MHD} source, and a Gadolinium choke was created to better adapt physiological monitoring technology for use in MRI. A smartphone-enabled portable device was prototyped to induce and measure V_{MHD} outside of the MRI, which offers a low cost, easy-to-use alternative to current methods of peripheral blood flow quantification. Finally, a phantom setup was constructed to explore contributing factors to induced V_{MHD} in a more controlled environment. Future work will continue to explore the different factors of V_{MHD} and test the developed technologies on larger patient groups.

INDEX WORDS: Magnetohydrodynamics, MHD Effect, Blood Flow, Electrocardiogram, ECG, Intra-MRI ECG, Smartphone

HEMODYNAMIC MONITORING: FROM MRI TO BEDSIDE

by

KEVIN JAMES WU

BS, University of Georgia, 2015

A Thesis Submitted to the Graduate Faculty of The University of Georgia in Partial Fulfillment of the Requirements for the Degree

MASTER OF ENGINEERING

ATHENS, GEORGIA

2017

HEMODYNAMIC MONITORING: FROM MRI TO BEDSIDE

by

KEVIN JAMES WU

Major Professor:	Tsz Ho Tse
Committee:	Changying Li
	Leidong Mao

Electronic Version Approved:

Suzanne Barbour
Dean of the Graduate School
The University of Georgia
August 2017

TABLE OF CONTENTS

Page

LIST OF TABLES

Page

LIST OF FIGURES

Page

CHAPTER 1

INTRODUCTION AND LITERATURE REVIEW

Magnetic Resonance Imaging (MRI) has been a staple diagnostic tool since it was posited as an extension of the existing Nuclear Magnetic Resonance (NMR) technique. Though the technology provides very high resolution and contrast of soft and hard tissues, there are challenges in its clinical use. The static magnetic field generated creates an environment where many of the current technologies utilized by clinicians, such as physiological monitors, are not viable.

One such physiological monitor is the electrocardiogram (ECG), an important diagnostic tool that shows the electrical activity of the heart, which allows clinicians and researchers to observe the condition of the heart. The ECG is a plot of voltage over time, showing the electricity generated by the heart over time. This means that the voltage changes observed in the ECG are indicative of the different parts of the cardiac cycle.

The cardiac cycle begins with the pumping of deoxygenated blood through the contraction of the right atrium into the right ventricle. The right ventricle then contracts and pumps the blood through the pulmonary artery into the lungs to become oxygenated blood. The oxygenated blood then flows back to the left atrium, which contracts to pump the blood into the left ventricle. Finally, the left ventricle contracts to expel all of the oxygenated blood into the aorta.

By convention, the main points of the ideal ECG waveform have been labeled by the letters P, Q, R, S, and T (Fig. 1). The P-wave indicates the start of the cardiac cycle, showing the voltage spike as the atria depolarize, contracting and pushing blood into the ventricles. The QRS complex, the largest, most prominent voltage spike of the ECG waveform, shows the electrical activity as

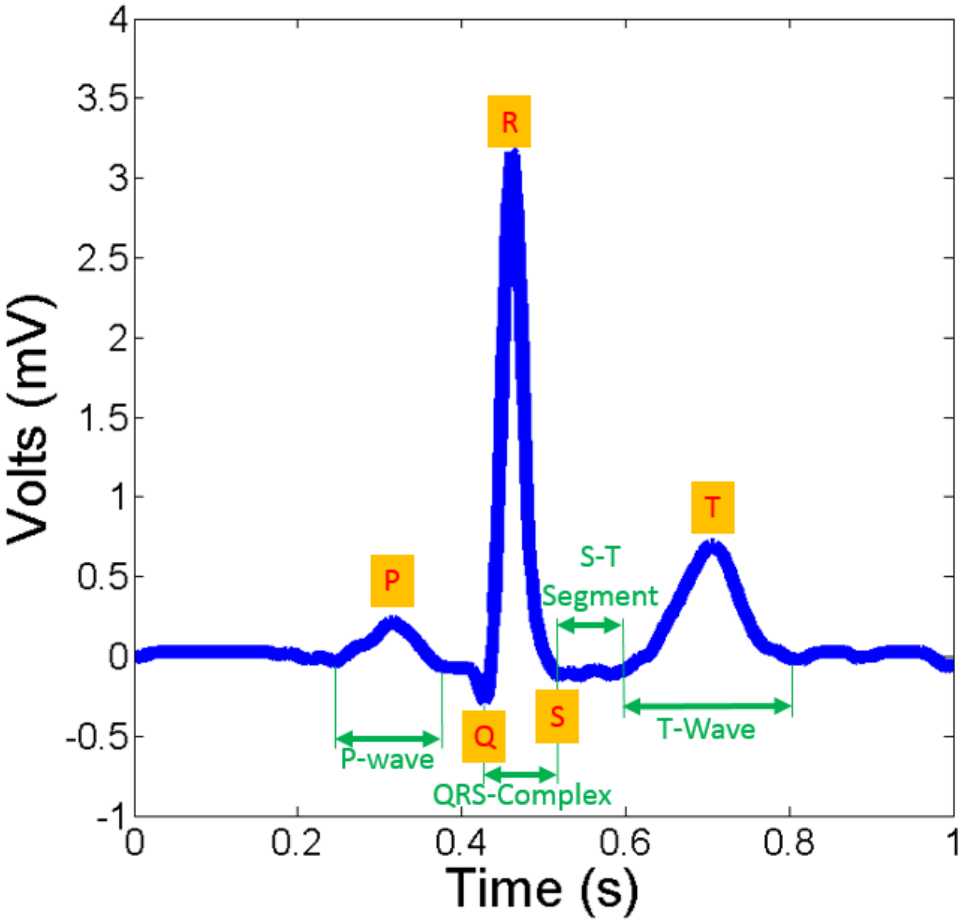

Figure 1.1: Diagram of a Single Lead Electrocardiogram

the ventricles depolarize, causing contraction and pumping deoxygenated blood to the lungs and oxygenated blood to the rest of the body. Finally, the T-wave corresponds to the repolarization of the ventricles, the relaxation and resetting for the next cardiac cycle. Atrial repolarization occurs as the ventricles depolarize, so the electrical activity is normally masked by the QRS complex.

In the field of Cardiac Magnetic Resonance (CMR), the most important tool to adapt for MRI compatibility is the ECG. ECG is utilized in cardiac gating, a technique developed to obtain motion-artifact-free cardiac images. Cardiac gating enables the MRI to synchronize the powering of the imaging coil to synchronize with the beating of the heart, to generate a clear image of the heart. Having clear intra-MRI ECG also allows for physiological monitoring of the patient, providing useful metrics for clinicians while also maintaining patient safety, which is paramount in human trials.

The main obstacle in obtaining clear intra-MRI ECG is the interaction between the blood flow and the static magnetic field of the MRI, most notably in the aortic arch [1, 2]. This interaction, the magnetohydrodynamic (MHD) effect, is the result of a Lorentz force, created by the charged blood (current) flowing perpendicularly to the field lines of the MRI's magnetic field. The force pushes the charged particles in the blood to a side of the vessel, creating a charge disparity, which registers as a voltage spike on the ECG. This voltage spike (V_{MHD}) is overlaid onto the ECG signal trying to be measured, resulting in a noisy signal that does not have many of the defining characteristics clinicians look for in the ECG waveform.

In mathematical terms, the MHD effect can be modelled by a simplified equation:

$$V_{MHD} = BLu \tag{1.1}$$

where u is the flow velocity, B_0 is the magnetic field strength, and L is the distance between electrodes, under the assumption that all the vectors are all orthogonal and uniform[3]. In the

case of intra-MRI ECG, the blood flow through aortic arch is perpendicular to the field lines of the MRI, causing a large V_{MHD} to be induced as blood is sent through the aortic arch, which occurs around the S-T segment and T-wave of the MRI. As an ECG measurement is a potential difference measurement, the induced V_{MHD} from all vessels oriented properly in reference to the magnetic field can contribute to the voltage measured between the two electrodes, such as in the case of the pulmonary artery, which also has blood flowing perpendicular to the magnetic field. However, due to the sheer size of the aorta compared to other vessels in the area, it can be called the main contributor to the induced V_{MHD}, while the contribution of the other vessels can be hard to even observe or validate.

Many recent studies strive to obtain clean ECG in intra-MRI conditions. In Tse et al., both hardware radiofrequency (RF) filtering and an adaptive software filter were used to eliminate noise from the intra-MRI ECG signals, yielding a less than 0.5mV peak-to-peak difference in ECG trace noise[2]. The study also noted the effect of RF noise on intra-MRI signals, which was combatted through use of shielded cables and ferrite chokes once the cables were outside of the 5-gauss line of the MRI. Another study conducted by Zhang et al. sought to remove noise from gradient-induced voltages through an equation giving the electric field, consisting of 19 coefficients derived from a linear regression of recorded data[4].

However, an interesting point came up in the discussion of the Tse et al. study, noting that the MHD voltage taken from the intra-MRI ECG could be potentially used to estimate stroke volume, which normally requires velocity encoded phase contrast (PC-MR) images to calculate in post processing[2]. Another study conducted by Nijm et al. gave a method for extracting the MHD voltage from intra-MRI ECG. 30-second ECG readings were taken both outside and inside the magnetic field of the MRI. The baselines of the signals were matched thorough high-pass filtering,

and QRS complex detection was used to sync up individual heartbeats. The two were then subtracted to yield the MHD voltage[3]. Now with a reliable method to isolate the MHD voltage, researchers could validate the correlation between stroke volume and the MHD voltage.

To test this theory, first it would make sense to create a model of the MHD voltages produced. In a study by Oster et al., three different models of MHD interactions with the aorta/aortic arch were examined[5]. The proposed model using 4D blood flow from PC-MR images was compared to both a theoretical model using the Navier-Stokes equation (using simplified assumptions such as a rigid vessel) and a geometric model using numerical analysis. The proposed model showed marked improvement in correlations (+5%), coefficient of determination (+1%), and fraction of energy (+22%) when compared to the "best previous model"[5]. While the proposed model only focuses on MHD contributions from the aortic arch, ECG was recorded in the thorax and therefore the assumption was viable.

This observation and correlation of V_{MHD} to stroke volume in a large patient study finally occurred in the work of Gregory et al [6]. V_{MHD} was obtained from the vectors of a vectorcardiogram (VCG), extracted using the subtraction methods from VCGs taken over 20-second breath-holds during elevated heart rate from exercise stress and after relaxation. In seven subjects, the V_{MHD} was used for subject-specific multiple-linear-regression (MLR) models of stroke volume; these models were validated with PCMR images of blood flow. Results showed a 7.22% error in SV estimation at elevated HRs and 3.69% error when relaxed through the aortic arch, showing a strong relationship between the stroke volume and measured V_{MHD} in the aorta.

However, the current methods of V_{MHD} extraction rely greatly upon the assumption that ECG_{Real} does not vary between the baseline ECG outside of the MRI bore and the intra-MRI ECG. A new methodology, using a pure source of V_{MHD} from the carotid artery as an input for a least

means square (LMS) adaptive filter, was devised to obtain ECG_{Real}. This project yielded a two-fold goal: (1) a different method for ECG_{Real} extraction from intra-MRI ECG, which could be implemented for better V_{MHD} noise removal in cardiac gating systems, and (2) a separate pure source of V_{MHD} on the body that could be further studied for its relation to stroke volume. The author implemented a 5-subject study to validate the use of the carotid V_{MHD} source as a "pure" V_{MHD} source and its ability as a LMS adaptive filter input to remove V_{MHD} noise from 12-Leads of intra-MRI ECG (Chapter 2).

An overarching issue that plagued has plagued the Medical Robotics Lab at UGA's research into intra-MRI ECG has been the modified MRI conditional ECG recorder being used for data acquisition. Commercial MRI-compatible ECGs are meant for diagnostic and monitoring purposes, and thus contain excessive filtering in order to create a signal usable by clinicians; however, when the research being done is investigating the noise induced in intra-MRI ECGs, such a system is not viable. The current MRI-Conditional ECG was limited in its uses in the MRI; specifically, no data acquisition could be done during scans as it would create image artifacts and ruin the scan results. To address this, the author helped create a choke-like device with a core made of a Gadolinium solution to attenuate the radiofrequency (RF) noise coming from the physiological monitoring devices to make the MRI-Conditional for use in the MRI, even during scans (Chapter 3).

Current studies have focused on the quantification of the stroke volume of the heart using the induced V_{MHD} on an intra-MRI ECG. However, at its base, the relationship being observed is regarding V_{MHD} and blood flow. The stroke volume of the heart is the total output of the left ventricle, which is all pumped through the aorta, the large vessel present within the area the voltage potential measurements are taken for ECGs. While stroke volume is an important clinical metric

for cardiovascular health and patient monitoring, blood flow in general, and through vessels other than the aorta, is also an important clinical metric.

Blood flow is a clinical metric with a variety of diagnostic uses, namely diagnosis and longitudinal monitoring of patients with or at risk of cardiovascular disease. Currently, blood flow can be quantified through several techniques, including Doppler Ultrasound (DUS), Computer Tomography (CT) and Magnetic Resonance Imaging (MRI). The majority of these methods require an expensive, immobile device (MRI, CT) and require a skilled technician to operate them (DUS, MRI, CT); thus, they are accessible to very few patients in need of the technology. Some of these technologies also expose patients to a range of discomforts, from the confined spaces in CT and MRI scans to the radiation exposure from CT and the radioisotope contrast agents used in MRI and CT. Based off this review of the current state of VMHD based flow, the author worked to create a portable, smartphone-enabled device that could record V_{MHD} and give blood flow metrics (Chapter 4).

With the creation of the device and a proof of concept for inducing V_{MHD} in peripheral vessels and outside of the strong magnetic field of the MRI, the next step was to further investigate how different factors, such as vessel thickness, flow rate, and magnetic field strength, effected the induced V_{MHD}. To this end, the author constructed a benchtop setup with two strong neodymium magnets with spacing to fit a custom flow channel in-between to conduct experiments (Chapter 5).

CHAPTER 2

ADAPTIVE FILTERING OF INTRA-MRI ECGS USING A DYNAMIC VMHD SOURCE

Having shown that the measured MHD Voltages are related to stroke volume, a more advanced study into the induced V_{MHD} in the MRI was warranted. To study the V_{MHD} induced in the blood vessels inside the MRI field would allow further insight into the nature of the relationship between blood flow and induced V_{MHD}.

As previously outlined, the current method of obtaining V_{MHD} involves a subtraction of the infected ECG from inside the MRI bore with a baseline ECG measurement taken outside of the MRI. The major drawback of this method is that it relies on separate measurements taken at different times. While interpolation can be used to temporally align the paired ECGs to adjust for variations in heartrate, it still relies on a preliminary baseline ECG in addition to post-processing to synchronize the ECGs for V_{MHD} extraction, ECG_{Real} filtering, and SV estimation. Currently, many different methods are used for the filtering of intra-MRI ECGs. It should be noted that most current methods revolve around at simple 4-Lead ECG for mostly gating purposes. Combinations of Fast Fourier Transforms (to find fundamental frequency of the MRI pulses added to the ECG) and band stop filters (to remove select frequencies of noise), along with template matching, among other methods, are employed to produce a cleaner intra-MRI ECG[7]. Independent Component Analysis (ICA), which is a statistical analysis to define underlying components to a signal assuming they are all independent of each other, has also been applied to intra-MRI ECGs to try to separate the V_{MHD} and ECG_{Real} signals; ICA was somewhat successful, though limited noise sources were used in the model, and simulated V_{MHD} was used[8-10]. A novel method was

hypothesized for ECG_{Real} extraction from intra-MRI ECGs, using a least means square (LMS) adaptive filter, trained by an external, dynamic source of "pure" V_{MHD} to filter out V_{MHD} noise in order to obtain clean ECG_{Real}.

To test this hypothesis, a proof of concept study was conducted to test validity of the source of pure V_{MHD} and the implementation of an LMS adaptive filter for ECG_{Real} extraction. The common carotid artery was selected for its physical isolation from the sinus node, close proximity to the body surface for external monitoring, and high flow rate. Conventional Velocity-Encoded Phase Contrast MRI (PCMR) was acquired in one healthy subject along the aortic arch and in the left common carotid artery.

12-lead ECGs were acquired during a 20-second breath-hold outside (Fig. 2.1a) and inside the MRI bore (Fig. 2.1b), while a secondary recorder was used to acquire a single bipolar anterior-posterior lead at the carotid artery. Blood flow was quantified in both the carotid artery and aortic arch by using PCMR (Fig. 2.2a); this was used to correlate raw carotidal lead signals with extracted aortic V_{MHD} from the 12-lead ECG.

During exercise stress testing, MRI-derived peak flow was shown to increase proportionally with an elevated heartrate in the ascending aorta and the common carotid artery, with an 8.49% difference in elevation between the two vasculature sources. V_{MHD} was shown to increase by 76.5% in the carotid artery and 88.1% in the aorta, illustrating a close correlation between carotidal and aortic derived MHD and flow (Fig. 2.2b), suggesting the ability of carotidal MHD to become an independent predictor for aortic MHD and an additional feedback term in modern ECG_{Real} extraction techniques during induced stress.

A correlation between the recorded carotidal V_{MHD} and the aortic V_{MHD} was shown and the potential to use raw carotidal MHD as a predictor of induced V_{MHD} was illustrated. This will

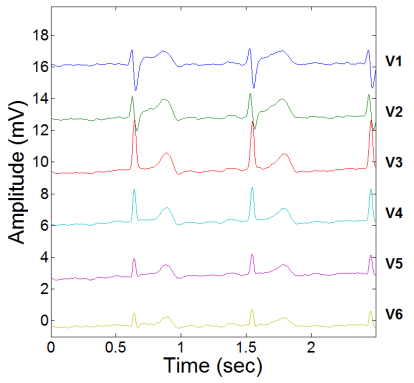

a) 12-lead ECG acquired outside the MRI

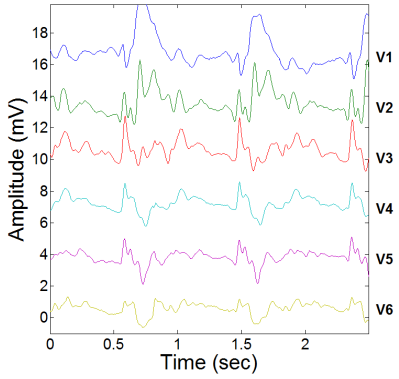

b) 12-lead ECG acquired inside the MRI (3T)

Figure 2.1: Observed V_{MHD} on Intra-MRI ECGs

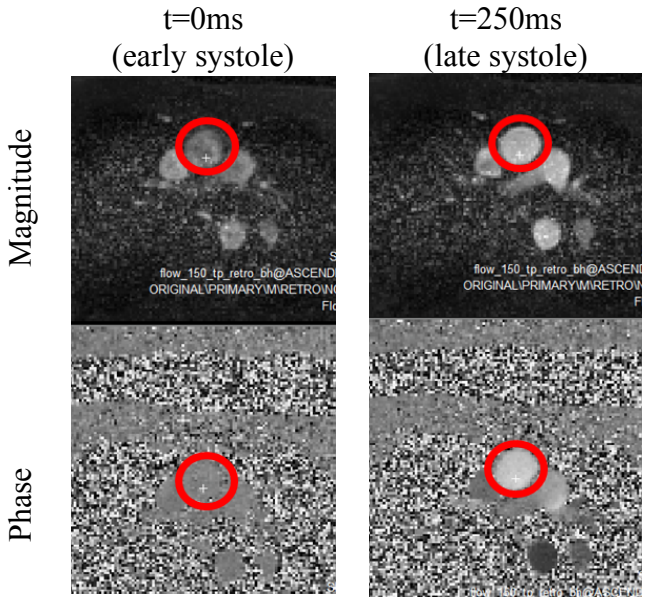

a) Phase Contrast MR (PCMR) images of the aortic arch used to estimate systolic flow during a resting heart rate: Magnitude (top) and Phase (bottom).

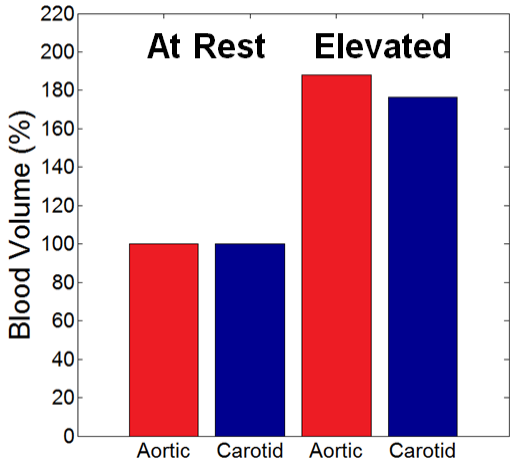

b) Increase in induced MHD during exercise stress testing in 12-lead ECGs and the carotidal lead, illustrating a 11.52% difference in carotidal and 12-lead elevation

Figure 2.2: Correlation between induced Carotidal and Aortic Magnetohydrodynamic Voltages (VMHD).

potentially allow for both the development of advanced methods of extracting ECG_{Real} and the acquisition of high-fidelity intra-MRI ECGs, which are essential in both imaging and patient monitoring applications.

With a suitable source of V_{MHD}, 12-Lead ECG data paired with carotid V_{MHD} measurements were taken for five healthy subjects (n=5). Both baseline measurements were outside of the MRI, and within the 3T magnetic field of a Siemens Skyra 3T MRI. 12-Lead ECG and Carotid V_{MHD} acquisitions were done over 20 second breath-holds to remove noise from muscle movements. 12-Lead V_{MHD} was extracted using the current subtraction method, after temporal alignment of the paired ECG measurements. The subtraction method was also used for Carotid V_{MHD} in order to account for any baseline changes in the signal in the two scenarios. The extracted V_{MHD} signals were scaled and then filtered through an LMS adaptive filter with 32 seeded coefficients and a 0.002 step size (Fig 2.3). Examination of the filtered ECG signal suggested that it seemed to be even noisier than the intra-MRI ECG signal, leading to questions about the efficacy of the filtering method. While there was a "bump" present in all three scenarios indicating the QRS complex, there was little else in the manner of clearly identifiable segments of the ECG waveform. To confirm, the correlation coefficients for all four subjects were calculated between the baseline signal and the filtered signal (Table 2.1). From the coefficients, it was obvious that there was very little relationship between the two signals, though the reasoning is not immediately apparent.

A single lead (Lead I) was isolated to observed the changes in signal from baseline to 3T MRI induced noise, to the filtered results (Fig. 2.4). Observing the single lead data, the most noticeable difference between the baseline and the other two sets was the large variance in amplitude. While the QRS complex voltages remain similar sized, the S-T segment and T-Wave

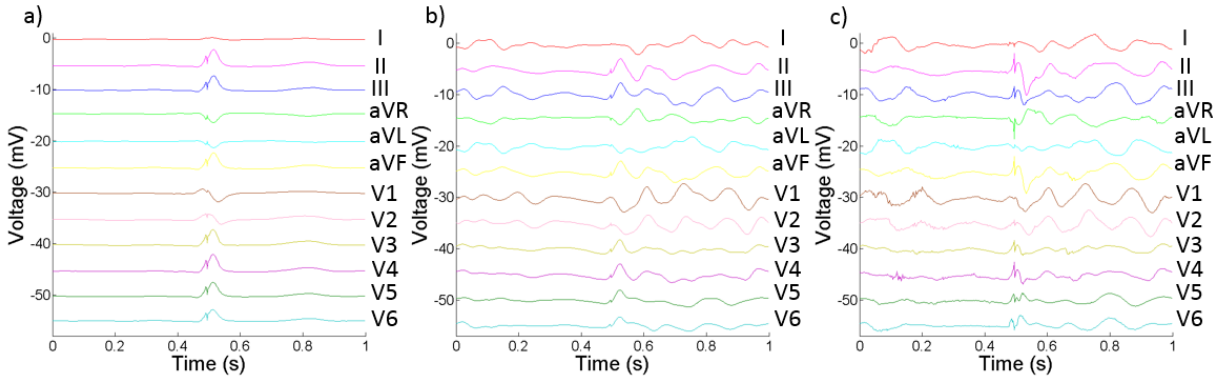

Figure 2.3: Comparison of 12-Lead ECG: a) Baseline, b) Inside 3T MRI, c) After Adaptive Filtering

Table 2.1: Correlation Coefficients of ECG_{Real} versus Adaptive Filtered Intra-MRI ECG

	Subject 1	Subject 2	Subject 3	Subject 4
Lead I	0.3012	0.1418	0.3807	0.1672
Lead II	0.3449	0.0838	0.3751	0.0424
Lead III	0.2068	0.0124	0.0174	0.0735
aVR	0.3727	0.1343	0.6336	0.1973
aVL	0.1434	0.1267	-0.0250	0.2173
aVF	0.1155	0.0606	-0.2101	0.0481
V1	0.3409	-0.0110	0.6095	0.3779
V2	0.5124	-0.1177	0.8939	0.3198
V3	0.5473	0.3611	0.8830	0.2014
V4	0.5371	0.1321	0.7840	0.1421
V5	0.4029	0.1547	0.7554	0.4525
V6	0.4799	0.0190	0.5947	0.5866

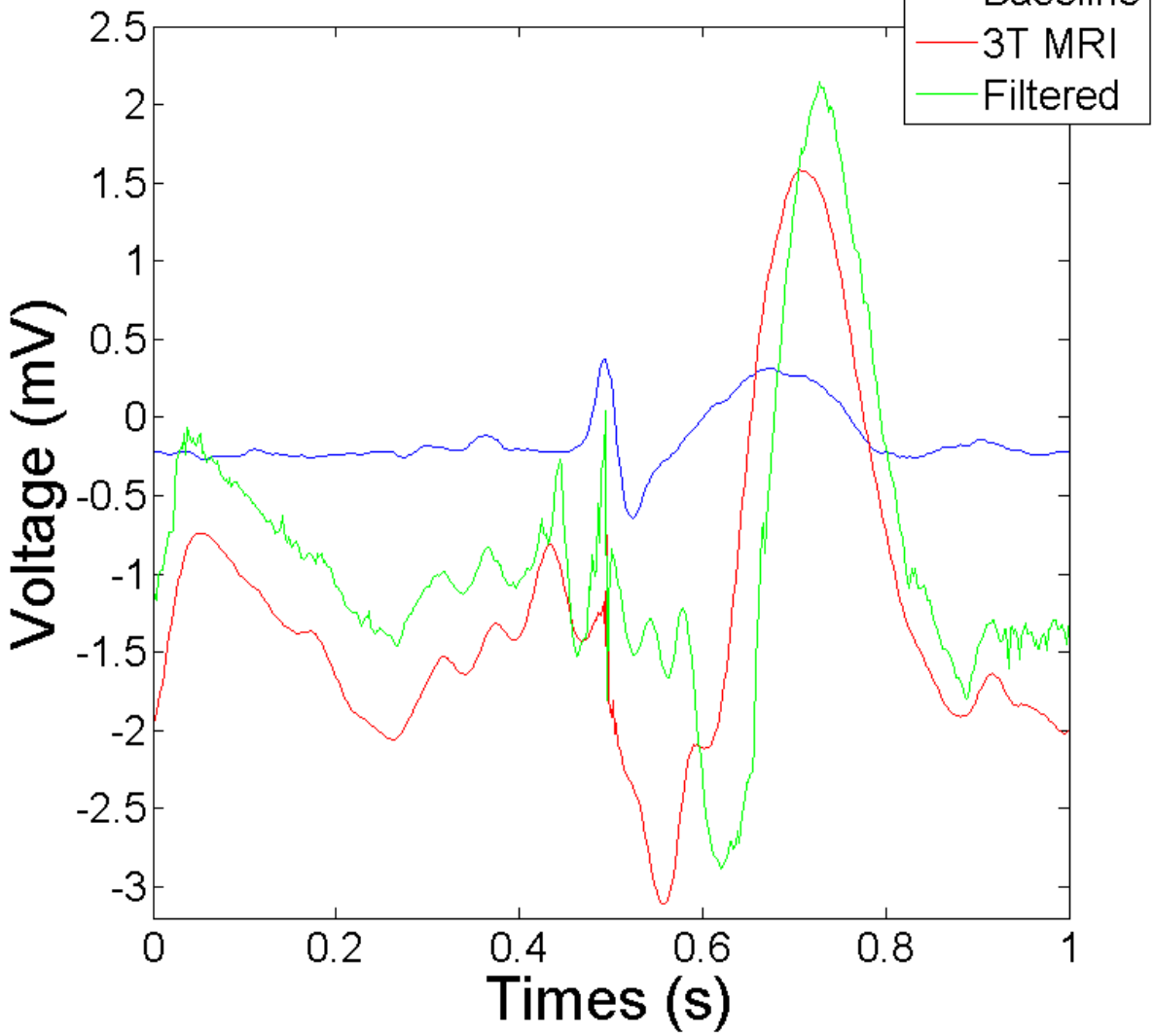

Figure 2.4: ECG Lead I from Baseline to 3T MRI, to Adaptive Filter.

were greatly increased in the intra-MRI measurement, which was expected, as this is the hallmark of V_{MHD} induced on the ECG waveform, as the S-T segment and T-wave occur as blood is being ejected into the aortic arch. However, the S-T segment and T-Wave elevation still being present in the filtered signal were not expected, which brings into question the V_{MHD} source used for the adaptive filter. The carotid V_{MHD} signal, while correlated to the induced aortic V_{MHD}, should have presented a large increase in induced voltage as blood flowed through the vessel, but due to its location, this happened at a later time than the V_{MHD} spike in a normal intra-MRI ECG waveform. Currently, this had not been accounted for in the segmentation process used for isolating ECG waveforms.

There was other evidence supporting this theory, as there was a definite temporal shift in the signals, as none of the waveform features properly lined up, even though the data was all normalized to 60 beats per minute. There was also misalignment when reconstructing the waveform, as seen in the peak of the QRS complexes among all three scenarios of the 12-Lead ECG. While these errors could have come from the resampling method used to convert the data all to the same rate, it was more likely a result of the segmentation method.

Although many issues plague the current adaptive filtering methodology, there is still promise in this work. In the future, work will be done to developing a more robust ECG segmentation method, and further data will be collected to better understand the time delays in registered V_{MHD} peaks at the aorta and carotid artery.

In the future, to test real-time implementation in the MRI, instead of requiring for the experiment two synchronized MRI-conditional ECG monitors, one to provide normal 12-Lead ECG and another to record the Carotid source of V_{MHD}, a single system could be developed and implemented, with 12-Leads + 1 Lead for the Carotid V_{MHD}. Further studies using this method on

larger populations would be required to standardize this as an alternative filtering method for Intra-MRI ECGs. Of particular interest are subjects present with cardiac conditions, such as arrhythmias, and the filter's ability to preserve the tell-tale ECG markers of the condition while still removing induced V_{MHD} noise. Another population of interest would be those present with carotid stenosis, and how this could affect the observed V_{MHD}. The results utilizing the LMS Adaptive Filter would also need reviewing from a clinical cardiologist to validate the diagnostic quality of the obtained ECGs. This adaptive filtering method would allow for eventual implementation of diagnostic quasi-real-time ECG in the MRI, allowing for better physiological monitoring of at-risk patient populations as well as improved cardiac gating.

CHAPTER 3

MAGNETIC RESONANCE CONDITIONAL PARAMAGNETIC CHOKE FOR SUPPRESSION OF IMAGEING ARTIFACTS DURING MAGNETIC RESONANCE IMAGING[1]

[1] Kevin J. Wu, T. S. Gregory, W. Zhao, R. Cheng, L. Mao, Z.T.H. Tse. Submitted to *Proceeding to the Institution of Mechanical Engineers, Part H: Journal of Engineering in Medicine*, 03/29/17

Abstract

Higher-risk patient populations require continuous physiological monitoring, and in some cases, connected life-support systems, during Magnetic Resonance Imaging (MRI) examinations. Most of these systems are connected to the outside using cabling that receives radio-frequency (RF) induction from the MRI's gradient and body coils during MRI scanning, resulting in excessive heating. We developed a passive method for RF suppression on cabling that may assist in making some of these devices MRI-compatible.

A barrel-shaped strongly-paramagnetic choke was developed to suppress induced RF signals which are overlaid onto physiological monitoring leads during MR imaging. It utilized a choke placed along the signal lines, with a Gadolinium (Gd) solution core. The choke's magnetic susceptibility was modeled, for a given geometric design, at increasing chelate concentration levels, and measured using a Vibrating Sample Magnetometer (VSM). RF noise suppression versus frequency was quantified with network-analyzer measurements, and tested using cabling placed in the MRI scanner. Temperature-elevation and image-quality reduction due to the device were measured using ASTM phantoms.

Prototype chokes with Gd solution cores exhibited increasing magnetic susceptibility and insertion loss (S21) also showed higher attenuation as Gd concentration increased. Image artifacts were observed on the phantom when the ECG was connect, though once the prototype choke was connected only a ~3% SNR variance was observed in the image when compared to a control. An accompanying temperature increase of $<1^{o}C$ was observed in the MRI phantom trial.

An effective paramagnetic choke for RF suppression during MR imaging was developed and its performance was demonstrated.

Introduction

During Magnetic Resonance Imaging (MRI) diagnostic procedures and image-guided interventions, real-time physiological monitoring and patient assist devices, such as defibrillators, are often required for the patient to be allowed to undergo the workflow, especially in the case of high-risk patients such as those with a history of ischemia or cardiovascular disease [11-13]. Single conductor and coaxial cables are often used to conduct these electromagnetic (EM) signals between probes on the subject and the accompanying bioinstrumentation [14]. In the environment of a MRI scanner, this presents a difficulty, as radio frequency (RF) signals are emitted from the MRI scanner during imaging and induce currents onto the cabling, superimposing relatively high voltages [14, 15]. These voltage overlays greatly reduce signal fidelity, can damage hardware and data acquisition systems, and result in excessive heating.

Clinical MRI scanning requires a large number of electrical cables, such as physiological signal leads, defibrillation pads, MRI surface coil cabling, RF ablation catheter cables, and various monitoring cables (SPO_2, strain), to be routed from the MRI bore to the scanner control room. Placing cables inside the MRI environment makes the system susceptible to multiple issues: (1) items made of ferromagnetic components may be displaced by the strong (1.5 or 3 Tesla) static field (B_0); (2) the magnetic-field gradients used in MRI imaging may induce waves in the cables (typically 20-9000 Hz); and (3) the MRI imaging sequence's RF pulses may induce Larmor frequency (typically 64 or 127 MHz) waves in the cables; and (4) imaging artifacts [16, 17].

Ferrite chokes are frequently used for suppression of the RF resulting from induced EM waves. They are largely constructed from ferromagnetic materials, mixtures of iron oxide particles with a secondary metal such as manganese or zinc [18-20]. Current flowing through a single conductor wound around a ferrite core produces a magnetic field inside the ferrite, which is

opposed by currents in the ferrite, attenuating the driving magnetic field. The currents in the ferrite dissipate once the inducing current subsides. As a result, Ferrite beads or cylinders are commonly mounted in several locations on electrical cables that traverse regions of high EM interference.

In the MRI scanner environment, ferrite chokes cannot be used in close proximity (>10 Gauss lines, typically) to the scanner since the strong static magnetic field saturates the ferromagnetic cores, rendering them less effective; there are also safety concerns due to the large forces exerted by the static field on the ferrites. Alternate solutions for reducing EM wave propagation do exist (resonant RF traps, active decoupling, and transformers) [21-23]. However, such approaches can be more difficult to implement and are more expensive than conventional ferrites. An inexpensive passive device, one that could be used in the MRI environment and provide effective RF suppression, would therefore by quite useful, as a partial or full replacement, for the tools currently employed.

Materials and Methods

A. Design Specifications

In order to design MRI-conditional passive devices which suppress high frequency (RF) induced currents from MRI gradient ramps during imaging procedures in a manner similar to a ferrite bead, three design constraints must be met: (1) the component must be able to be used safely inside and in close proximity to the MRI scanner [24]; (2) the magnetic moment of the component must not saturate in the MRI static magnetic field [25, 26], thereby maintaining efficacy inside and outside of the MRI bore; and (3) large currents flowing on the cables must be dissipated in the device to avoid patient thermal injuries [27-29].

In addition to the above design specifications for RF suppression in the MRI environment, the resultant device must meet practical geometric shape and size constraints in order to easily

mate with standardly-used cabling. The device must also allow un-inhibited propagation of the desired signal waveforms. Typical examples are cabling used for Electrocardiogram (ECG) recording (0-200Hz), or external defibrillators (20-300Hz). Another specification that must be taken into consideration is the artifact size of the choke in MR images, which would ideally be small (under ~5mm).

B. Magnetic Susceptibility of Gadolinium Chloride

As ferrite beads or cores are traditionally used for RF suppression in cabling, this study searched for a non-magnetic alternative with similar suppression capabilities. Strongly paramagnetic materials, with a relatively high magnetic susceptibility, were prime targets. Liquid solutions, such as liquid ferro-magnets used in high power commercial transformers, seemed to be a good choice due to their manageable paramagnetic material concentration, ability to be placed in the core of a wound solenoidal inductor, and ability for dissipating heat easier than solids. Since chelated forms of the Gadolinium ion (Gd) are commonly used as MRI contrast materials (for perfusion or angiography purposes) as a result of their large magnetic susceptibility (χ), they were a natural choice.

Gd as a free ion is highly toxic; however, as a chelated compound (a metallic ion bonded to organic ligands) it is biologically safe. Typically, chelated forms of Gd such as Gd-DTPA, which is found in commercially available Magnevist (Gadopentetate Dimeglumine, Bayer, Whippany, NJ) [30, 31], preserve the paramagnetic effect of the Gd ion. However, Magnevist has limited solubility compared to the free ion form. The toxicity of free Gd ions, which is due to interactions with calcium channel dependent processes, requires approximately 100-200 mg/kg to become a 50% lethal dose. As a result, we surmised that we could utilize a substantially lower

dose of the ionic form, and still achieve the desired paramagnetic effect within a small-volume paramagnetic choke.

Gadolinium (III) Chloride ($GdCl_3$) was chosen for the paramagnetic core due to its high solubility in water. In order to determine the optimal concentration, Magnevist was chosen as a median point, with approximately 131.8 mg/mL of $GdCl_3$ yielding the same amount of paramagnetic Gd as commercially available Magnevist [30, 31]. Four concentrations of the Gd ion were examined based on the commercially available concentration: (1) 0 mg/mL; (2) 66 mg/mL; (3) 132 mg/mL; and (4) 198 mg/mL.

A Vibrating Sample Magnetometer (VSM) [32, 33] was used to assess magnetic susceptibility by magnetizing the sample in a uniform magnetic field ($\vec{H}$ kA/m) and measuring the material magnetization ($\vec{M}$, A/m) [32-34]. Based on this relationship, the bulk magnetic susceptibility (dimensionless) was calculated (Eqn. 3.1).

$$\chi = \vec{M} \Big/ \vec{H} \tag{3.1}$$

C. Choke design and MRI artifact estimation

In order to determine suitability for the MRI environment and maximize the inductor (choke) efficacy while reducing the extent of the magnetic field generated beyond the physical dimensions of the device, which would result in MRI image artifacts, the magnetic field of the prototype device was simulated using the Biot-Savart law [35, 36]. The Biot-Savart law describes the magnetic field $\vec{B}$ at position $\vec{r}$ in the free space generated by a wire *C* with electrical current *I* (Eqn. 3.2).

$$\vec{B}(\vec{r}) = \frac{\mu_0}{4\pi}\int_c \frac{Id\vec{l}\times\left(\vec{r}-\vec{l}\right)}{\left|\vec{r}-\vec{l}\right|^3} \tag{3.2}$$

where μ_0 is the magnetic permeability of free space, $\vec{l}$ is the position vector of an elementary segment of wire and the current vector in it is $Id\vec{l}$. As a result, the pointing vector from $\vec{B}$ to the elementary current $Id\vec{l}$ is $\vec{r}-\vec{l}$. From Eq. 2, the magnetic field $\vec{B}$ has contributions from all the current elements within the wire *C*. When the wire is wrapped in a solenoidal pattern onto a cylindrical core of magnetic permeability μ, it becomes an inductive coil and the distribution of its induced magnetic field $\vec{B}$ can be calculated according to Eq. 2 and expressed in Cartesian coordinates [35-37] (Eqn. 3.3).

$$\vec{B}(x,y,z) \tag{3.3}$$
$$= \frac{\mu nIR}{4\pi}\int_0^L\int_0^{2n} \frac{\hat{\imath}(z-L)cos\theta + \hat{\jmath}(z-L)sin\theta + \hat{k}(R-ysin\theta - xcos\theta)}{[(x-Rcos\theta)^2+(y-Rsin\theta)^2+(z-L)^2]^{3/2}}d\theta dL$$

where *R* is the radius and L is the length of the coil, and *n* is the number of turns in one-unit length of the coil (Fig. 3.1a).

Looking at the simulation results, the magnetic field decayed for 1-2mm past the edge of the choke dying down to less than 5% by 3mm from the edge compared to the ambient background, leading to a predicted artifact extensions of the same size (Fig. 3.1b). Based on the simulation, a paramagnetic core inductor was constructed using 15 AWG gage copper (magnet) wire wound parallel to a 1cm diameter Polytetrafluoroethylene (PTFE) tube containing 3mL of the Gd solution at each of the three concentration levels (Fig. 3.1c). Adjacent loops were spaced at 2 mm

a) Shape of a solenoidal inductor used to compute the magnetic field according to the Biot-Savart law, where R and L are the radius and length of the coil, and n is the number of turns.

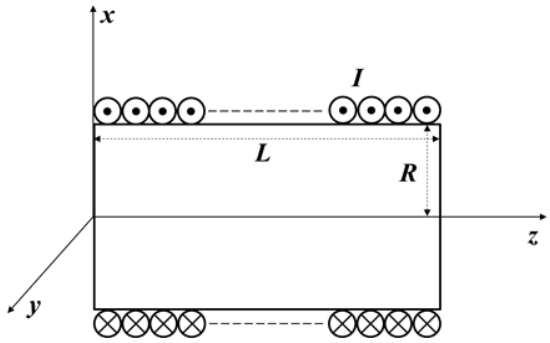

b) Simulated magnetic field of the paramagnetic core inductor (top). The magnetic field is shown to rapidly deteriorate 1-2 mm radially from the external wires in the enlarged view (bottom).

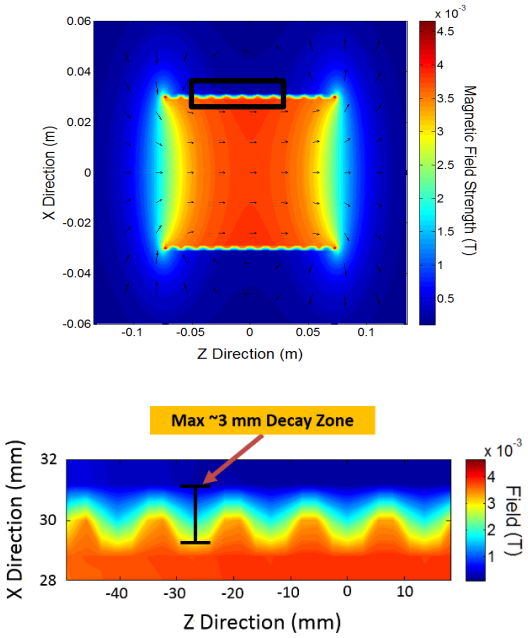

c) Dimensional (mm) CAD drawing of the prototype barrel choke assembly before insertion of the SMA end connectors and the paramagnetic core solution.

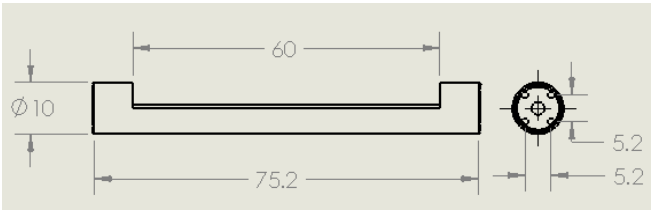

d) Prototype (left) and CAD design (right) of a barrel choke assembly to house the paramagnetic core inductor. SMA connectors are at both ends.

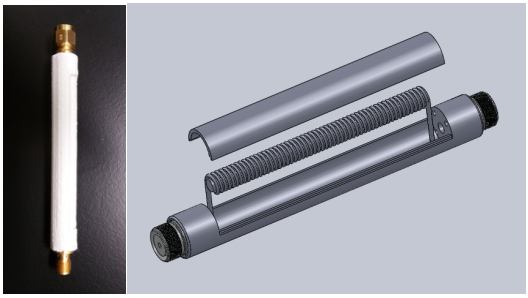

Figure 3.1: Design of a paramagnetic core solenoidal RF suppression barrel-choke.

increments to reduce parasitic capacitance. External physical dimensions of the inductor were an outer diameter of 1.3 cm and a length of 6 cm. The solenoid assembly was placed in a rapid-prototyped "barrel-choke" shaped case containing SMA input and output RF connectors (Fig. 3.1d).

The RF performance of the Gd solutions was evaluated using a 1.3 GHz Vector Network Analyzer (VNWA) (SDR, Wiltshire, UK). The VNWA characterized the 2-port scattering parameters, with incident power into the device at ports 1 and 2 (a1, a2), and power exiting power in ports 1 and 2 (b1, b2) (Eqn. 3.4).

$$\begin{bmatrix} b_1 \\ b_2 \end{bmatrix} = \begin{bmatrix} S_{11} & S_{12} \\ S_{21} & S_{22} \end{bmatrix} \begin{bmatrix} a_1 \\ a_2 \end{bmatrix} \tag{3.4}$$

S21 can be analyzed to obtain insertion loss over the choke in attenuation RF at the 3T Larmor frequency (~128MHz).

D. Performance during MR Imaging

The Gd ion barrel-choke solution was designed for use with an MRI-conditional ECG acquisition system [11-13, 38] (Fig. 3.2a). Suppression of RF energy was assessed through monitoring of thermal and image SNR effects were quantified in a 3T MRI American Society for Testing and Materials (ASTM) standards [39, 40] (Fig. 3.2b). A saline-filled human torso NEMA phantom was designed and constructed for placement in the MRI scanner. The temperature increase in the phantom was measured during MRI scans.

Image artifact dimension was defined as a ≥ 30% change in pixel intensity in three test scenarios: (1) a control of just the phantom; (2) the phantom with ECG system attached; and (3)

a) Gd ion barrel-chokes placed on four channels of an MRI-conditional ECG recorder.

b) Experimental design for testing the thermal effects and image SNR resulting from the choke.

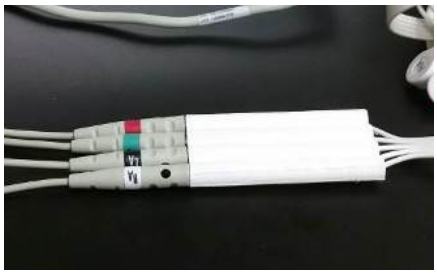

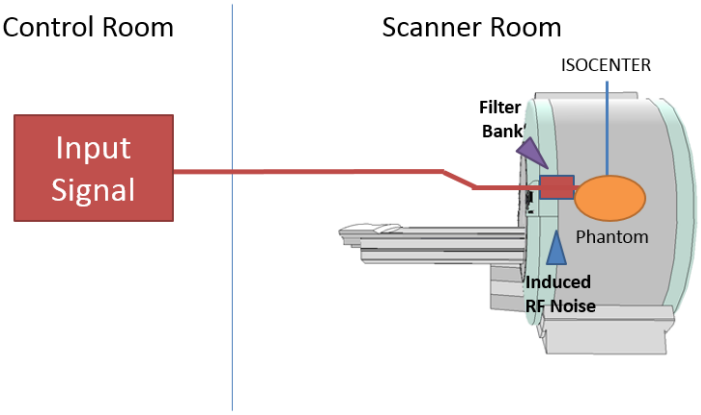

Figure 3.2: Evaluation of the performance of the Gd ion barrel-choke in the presence of an external RF source (127.74 MHz).

the phantom with the ECG system attached with the choke inserted inline. Comparison was made between before (baseline) and after the introduction of the choke [40]. From acquired MRI images, SNR was measured as the ratio of the mean intensity value within a 40 pixel x 40 pixel region at the center of the image (I_{center}) and the standard deviation of intensity values obtained in a 40 x 40 region in the image corner (SD_{corner}) (Eqn. 3.5).

$$SNR = \frac{I_{center}}{SD_{corner}} \tag{3.5}$$

Results

A. Magnetic Susceptibility of Gadolinium Chloride

The $GdCl_3$ solution susceptibility was characterized using the VSM for the following concentrations (1) 0 mg/mL; (2) 66 mg/mL; (3) 132 mg/mL; and (4) 198 mg/mL. An increase in magnetic susceptibility of the $GdCl_3$ solution was observed as the ion concentration in the solution increased (Fig. 3.3). An increase in magnetic susceptibility of the solution was observed as the concentration was increased. There was also close agreement of the magnetic susceptibility obtained experimentally to the simulation performed for the same concentrations (<2% error). The susceptibility observed at the two highest concentrations did not change dramatically, suggesting a plateau in performance as the solution neared saturation.

B. Choke design and MRI artifact estimation

From the simulated inductor, the magnetic field of the energized coil was simulated using the 198 mg/mL paramagnetic solution and a specified magnetic susceptibility of 73.6. The generated magnetic field was predicted to rapidly deteriorate with increasing distance from the center, which

a) Magnetization and field strength characterization of $GdCl_3$ obtained from VSM at each concentration level.

b) Bulk magnetic susceptibility of the Gd ion solutions as a function of concentration calculated from the VSM output.

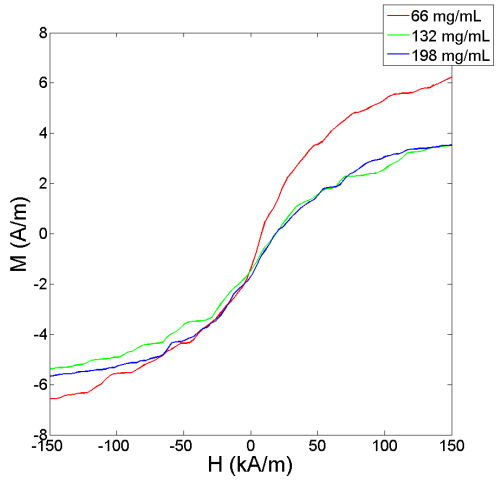

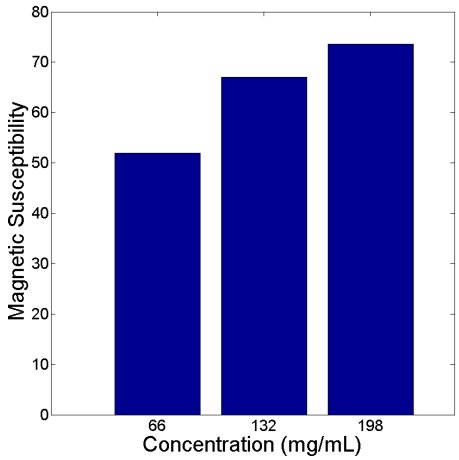

Figure 3.3: Magnetic Susceptibility of $GdCl_3$ solution under varying Gd ion concentrations.

should generate imaging artifacts only at distance of <2 mm (Fig. 3.1b) further from its physical boundary (radius).

Scattering parameter characterization of paramagnetic core inductive chokes was performed using the vector network analyzer, illustrating the practical performance of the device with frequency (Fig. 3.4). Examining the insertion loss (S21) of the prototype chokes, the chokes with $GdCl_3$ solution cores demonstrated much greater signal attenuation as frequency increased when compared to the control (water core). Insertion loss further increased with concentration with the control (water) presenting a loss of 17dB, and a loss of 23 dB, 26 dB and 29dB for the 66mg/mL, 132 mg/mL, and 198 mg/mL solutions, respectively, at the Larmor frequency. These results lead to the 198mg/mL solution being chosen as the most viable paramagnetic solution to use as an MRI conditional passive RF suppression choke for its high signal attenuation.

C. Performance during MR Imaging

During the phantom studies, an average temperature increase of 0.5^{o}C was observed with no Gd ion barrel-chokes attached to the electrodes, while an average temperature decrease of 0.3^{o}C was observed with the Gd ion barrel-chokes in-line with the electrodes over the course of a full 10 minutes of MR imaging (Fig. 3.5). Image SNR and susceptibility artifact size were quantified by connecting the choke to the phantom and introducing it into the region of interest, respectively (Fig. 3.6). Particularly of note were the artifacts induced by the ECG, present near the bottom of the Phantom (Fig. 3.6b). When the prototype choke was added in-line to the ECG cables, the previously observed noises were immediately visible on the image (Fig. 3.6c). The SNR variation between the control image (Fig. 3.6a) and the image with the prototype choke (Fig. 3.6c) was ~3%.

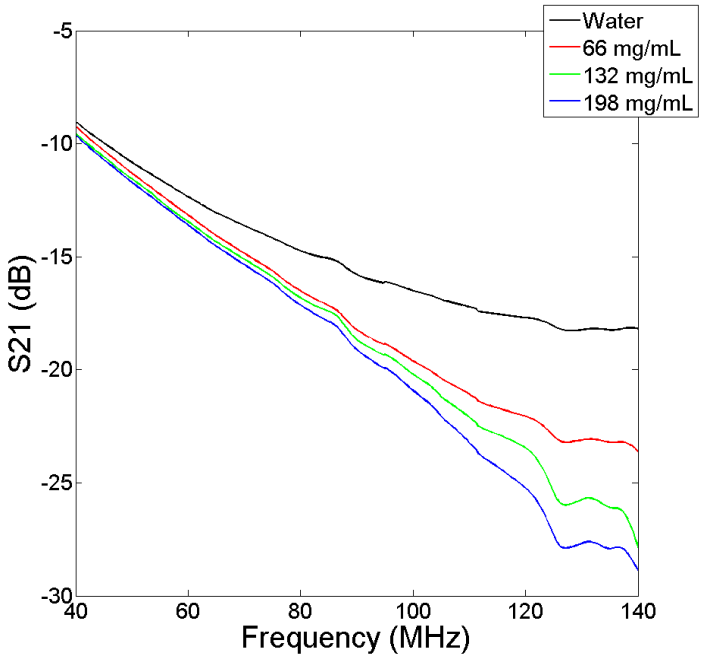

Figure 3.4: Scattering Parameter characterization of $GdCl_3$ solutions

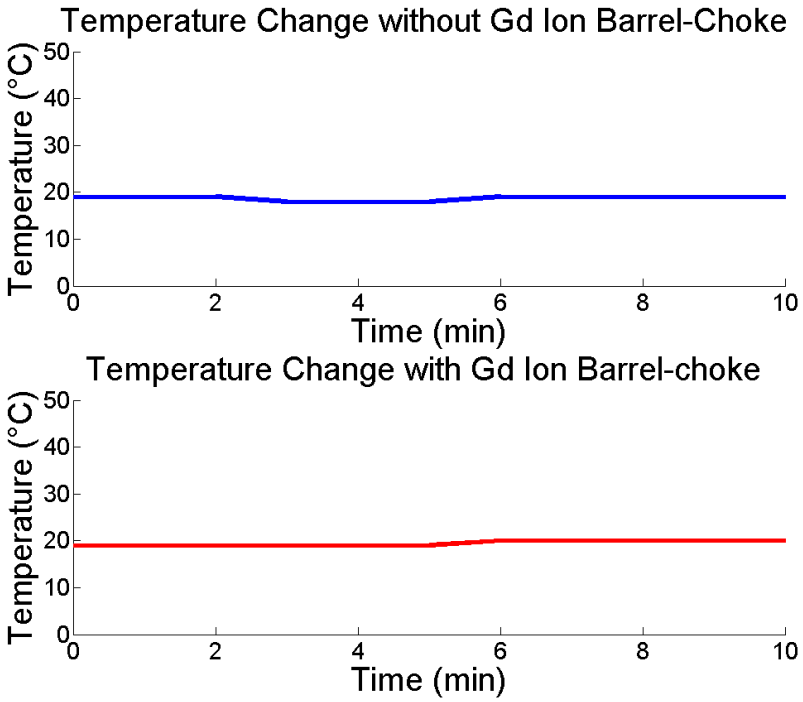

Figure 3.5: Thermal heating effects of Prototype Choke over a 10-minute scan

a) Control

b) ECG Recording

c) ECG Recording w/ Prototype Choke

Figure 3.6: Performance of prototype choke during MR Imaging

Discussion

The susceptibility of the device was experimentally measured using Vibrating Sample Magnometer (VSM), which demonstrated increasing susceptibility and observed increase in insertion loss as Gd ion concentration increased. The simulation also quite accurately predicted the choke's effects on MRI images in terms of image artifacts generated, which was minimal. When comparing the image of the phantom connect to the ECG without (Fig. 3.6b) and with the prototype choke (Fig. 3.6c), there was the immediately obvious image artifact in the bottom right corner when the ECG was connected without the prototype choke (Fig. 3.6b). By contrast, there was little observable visual artifacts on the image of the phantom with the prototype choke attached (Fig. 3.6c), as well as a small SNR variance when compared to the control image, demonstrating the ability of the prototype choke to mitigate RF noise from physiological monitoring electronics, and the role the choke could play in the adapting of different monitoring solutions for MR-Conditionality. The choke also was shown to have minimal thermal effects in the phantom test, suggesting that the device was MRI-conditional. However, it is also important to note that very little temperature variance was noticed when the ECG was connected to the phantom without and with the prototype choke, though there was less temperature change observed with the prototype choke inline.

The device may enable research and development of MRI-conditional devices that may not be currently unavailable due to design or cost constraints. The use of the presented device maintains a low cost and level of affordability. In order to encourage adoption of the presented paramagnetic choke, further work should be performed to ensure that the presented design specifications can be met for a wide range of in-room MRI devices and MRI magnetic strengths.

The study itself was focused on quantifying device parameters, and was conducted on the benchtop or with phantoms; pending IACUC approval, further testing with animals under a variety of MRI field strengths and sequences will be performed to further evaluate the choke performance in RF suppression and its thermal effects on subjects. The three concentrations of Gd solution tested as cores for the choke were not comprehensive, and further optimization of the Gd solution used could help optimize RF suppression.

In conclusion, the design of a passive paramagnetic RF choke was tested with a network analyzer to evaluate for its insertion loss performance. Experiments were conducted in 3T MRI to demonstrate minimal artifacts generated from the choke design as well as minimal heating effects.

CHAPTER 4

MAGNETOHYDRODYNAMIC VOLTAGE RECORDER FOR COMPARING PERIPHERAL BLOOD FLOW

Introduction

Electrocardiography (ECG) is commonly employed as a bedside clinical tool used to assess abnormalities in cardiac electrical activity. As a result of this, coupled with the advent and rise of smartphone-enabled devices, an era of digital medicine has begun to embrace this technology [41, 42]. A number of commercial outlets have emerged which offer portable ECG monitors which feature wireless connectivity and advanced data storage and sharing options [43-47]. These new technologies allow for more convenient longitudinal patient monitoring, detection of cardiac events [48, 49], and intuitive data-logging to track cardiac activity for an overseeing physician [50, 51].

Portable ECG monitors offer many new potential diagnostic and monitoring opportunities; however, they become limited by concentrating on ECG-based diagnosis. One clinical metric which could benefit from portability is blood flow. In intra-MRI ECG, voltage overlays (V_{MHD}) have been observed, due to the interaction between the magnetic field of the MRI and the blood flow in the body, through the magnetohydrodynamic (MHD) effect. The effect is primarily observed in the aortic arch during the ST segment and the T wave and has been successfully recreated in computer simulation [52]. The V_{MHD} observed has been shown to be indicative of blood flow [2, 6, 53, 54]. By reproducing this effect with a static magnet outside of the MRI, a different modality of flow monitoring could be developed using portable ECG monitors.

The need for an alternative flow assessment modality, particularly a more portable one, is great. In the United States, 85.6 million adults are affected with cardiovascular disease, and of that group, 8.5 million are afflicted with Peripheral Artery Disease (PAD) [55]. The blood flow metric could be very useful as a metric for monitoring cardiovascular health, especially in cases of peripheral circulation, and could also serve as an indicator of wound healing [56-62] The current method for diagnosing PAD is the Ankle-Brachial Index (ABI)[63]. The ABI is a simple test where the blood pressures of the arm and ankle are compared to determine the state of peripheral arterial health. However, in cases when a likely PAD diagnosis is made further investigation into peripheral blood flow must be made. Current methods for measuring blood flow are quite costly, requiring either skilled technologists to operate or expensive, immobile equipment. A portable ECG based method for flow monitoring would allow for an inexpensive and more layperson-friendly method of acquiring flow data.

The MHD Effect is a widely observed physical phenomenon, with a recent emergence into the field of medicine and cardiology [2, 64, 65], known to occur from strong magnetic field ($\overrightarrow{B_0}$) interactions with rapidly flowing conductive fluid of velocity $\vec{u}$ over the distance vector $\vec{L}$ across a pair of measurement electrodes (Eqn. 4.1).

$$V_{MHD} = \int_0^L \left(\vec{u} \times \overrightarrow{B_0}\right) \cdot \overrightarrow{dL} \tag{4.1}$$

Initially, the phenomenon was observed in the human body through V_{MHD} overlays on ECG recordings acquired within the strong magnetic field of a Magnetic Resonance Imaging (MRI) scanner (B_0) (Fig. 4.1) [66, 67]. This overlay was found to correlate well with arterial blood flow [1, 5, 68], and has been employed to estimate left ventricular stroke volume during a conventional MRI workflow [13].

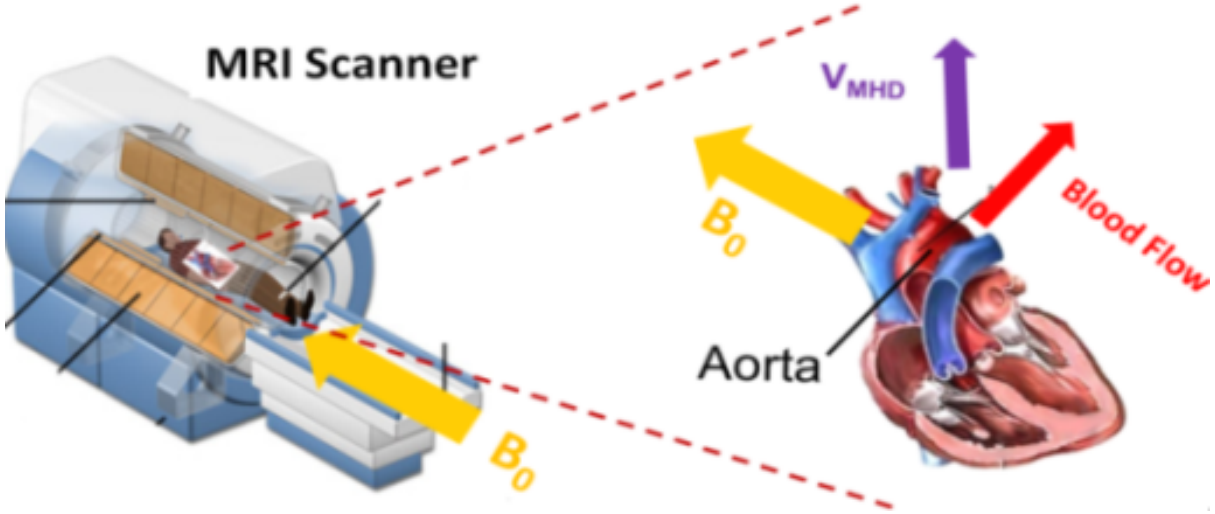

Figure 4.1: Principle of the MHD effect as induced upon major vasculature inside an MRI scanner.

In the presence of B_0, typically 1.5 to 3 Tesla in strength, induced V_{MHD} can oftentimes eclipse the true QRS complex in ECG recordings (Fig. 4.2) [64, 69]. Through the development of a stand-alone platform, the external magnetic field would need to be reduced in magnitude to maintain portability, while still providing a measurable V_{MHD} overlay. Preliminary work has been performed into the scaling of this effect using an embedded permanent neodymium magnet ($B_{r,\,max}$ = 0.4T) for V_{MHD}-derived physiological monitoring [70].

With the large adoption rates of smartphone technology, it follows that technology would be developed to enable wider applicability in the healthcare field [71], and as such, a larger trend is beginning to emerge, in which portable, low-cost, and non-invasive health monitoring devices are becoming more desirable [72, 73], with less needs for considerations regarding external communication [74, 75], and remote/long-term powering [72, 76].

Due to these modern trends, we aim to bring this V_{MHD} based blood flow measurement outside of the MRI by developing a portable smartphone-enabled ECG recorder capable of performing rapid peripheral blood flow measurements using V_{MHD}-derived techniques induced by static magnets, with direct applications to the field of digital medicine.

Materials and Methods

In order to translate the observed MHD effect from the environment of the MRI scanner to that of a portable, hand-held device which can be used distally from the heart and on peripheral vasculature, a device was designed and validated based on the scaled effect in three core parts: (1) design of a smartphone-enabled ECG monitor; (2) characterization of the scaled MHD effect; and (3) device validation under varying heart rates (HR).

In order to design a portable ECG monitor, which is capable of meeting current standards regarding the derivation and display of ECG traces, design emphasis was placed with regards to

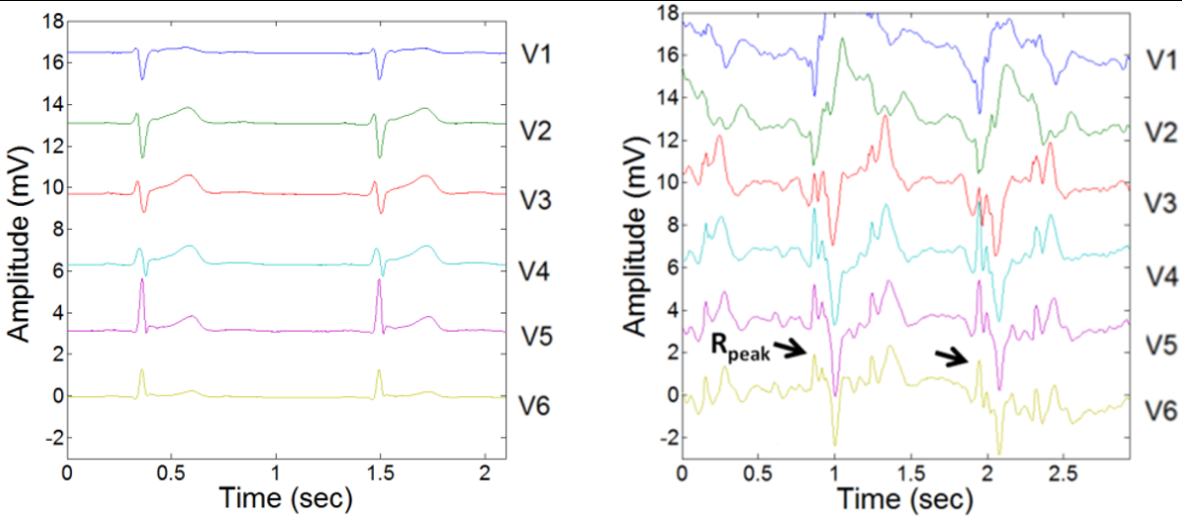

Figure 4.2: Induced VMHD overlay on recorded ECGs in the environment of a MRI scanner.

meeting current American Heart Association (AHA) recommendations for the standardization and interpretation of the ECG [77]. A single-lead approach was selected to reduce system complexity and hardware requirements.

A minimum frequency bandwidth of 0.05 Hz to 150 Hz, commonplace in commercially available multiple lead ECG systems as per AHA guidelines [77], was established to remove possible high frequency noise and to reduce baseline drift [78]. A sampling rate of 1500 samples per second was chosen as the expected V_{MHD} induced would be small variances in the waveform, so oversampling was required [79, 80]. A second order digital zero-phase notch filter was implemented to remove induced 60 Hz line noise which may occur. This configuration was considered advantageous as compared to a large number of portable ECG monitors which commonly utilize a non-standard low-pass bandwidth (typically 40 Hz), resulting in improper ECG filtering and potentially adverse clinical consequences [77, 78]. In addition, as the proposed system acquires only a single ECG lead, traditional compression techniques to ensure a stable sampling frequency were unnecessary [81, 82].

A conventional bio-instrumentation hardware approach was taken to acquire and digitize ECG traces (Fig. 4.3).

A low-power, high-impedance (10^{10} Ω) differential-input instrumentation amplifier (INA128p, Texas Instruments, Dallas, TX) was selected as the device front-end with a gain of 200 for its high common mode rejection (120 dB at a gain > 100), input protection/buffer amplifiers, and low drift/offset. The exceptionally high input impedance of the instrumentation amplifier also allowed for use in a wider variety of subjects and areas, as it would lessen the impact of the varied impedance caused by differences in body composition and measuring locale.

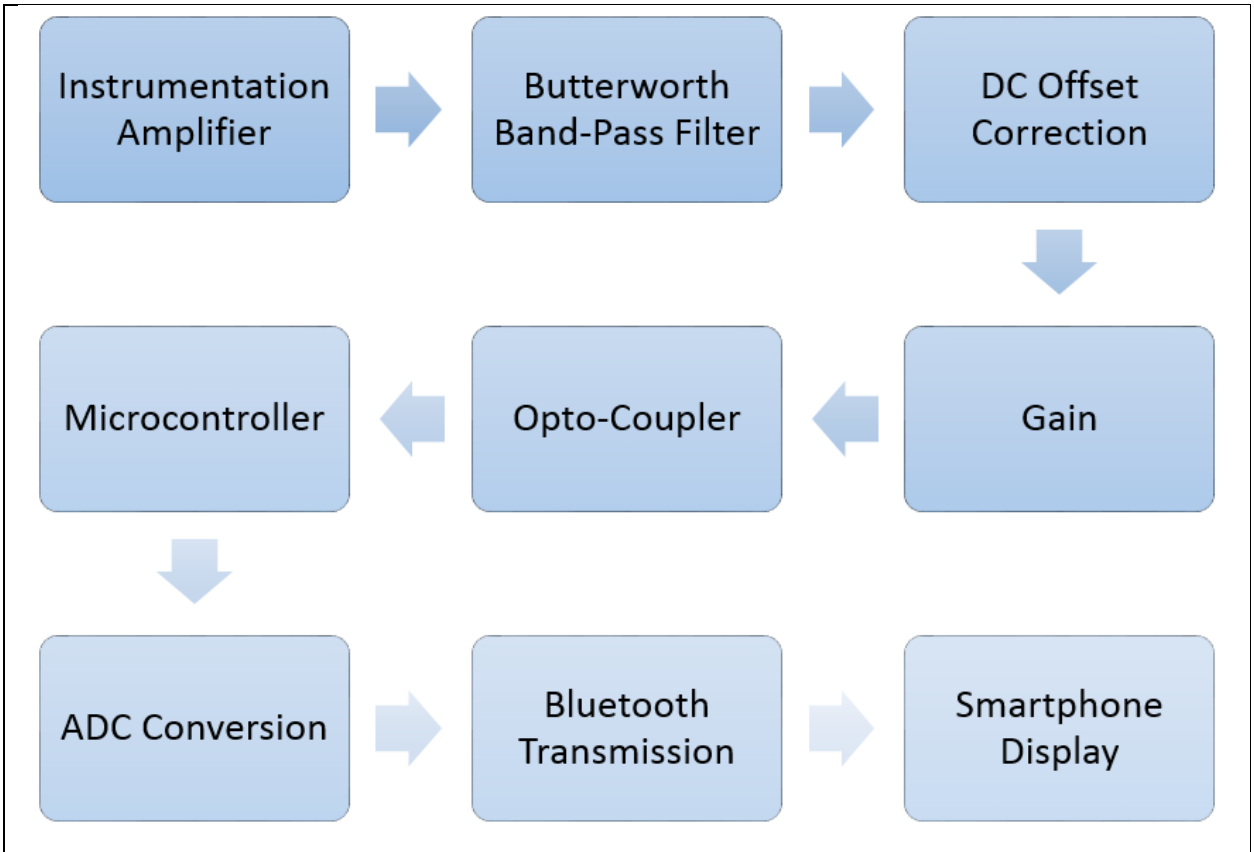

Figure 4.3: Single-lead ECG acquisition system block diagram.

An industry standard gain equation based on a single external resistor was used to set the front-end gain, which aids in reducing signal drift and increasing the common mode rejection by allowing for precision laser-trimmed resistors to balance the circuit (Eqn. 4.2).

$$G = 1 + \frac{50k\Omega}{R_G} \tag{4.2}$$

A Sallen-Key 4-pole Bandpass filter was designed with a Butterworth frequency response to enforce the prescribed frequency bandwidth, and serve as an anti-aliasing filter. A Butterworth frequency response was selected to maintain a maximally flat passband and reduce ECG distortion, whereas the gain can be described as a function of angular frequency (ω) and the number of poles (n) (Eqn. 4.3).

$$G(\omega) = \sqrt{\frac{1}{1 + \omega^{2n}}} \tag{4.3}$$

Implementation was performed by cascading individual 2-pole high and low pass sections. Through using equal resistance values, the Q-factor and cut-off frequency (ω_0) in each 2-pole filter, such as in the low-pass section, can be reduced from its original form taken from the transfer function (Eqn. 4.4) to simplified expressions (Eqn. 4.5, 4.6).

$$H(s) = \frac{1/R_1R_2C_1C_2}{s^2 + s\left(\frac{1}{R_2C_1} + \frac{1}{R_1C_1}\right) + 1/R_1R_2C_1C_2} \tag{4.4}$$

$$Q = \frac{1}{2}\sqrt{\frac{C_1}{C_2}} \tag{4.5}$$

$$\omega_0^2 = \frac{1}{R_1R_2C_1C_2} \tag{4.6}$$

A dual op-amp DC-offset correction, utilizing a single op-amp differential amplifier and a simple gain stage were subsequently implemented prior to an isolation opto-coupler to serve as the analog output. The total gain of the system was set to 500.

The output of the analog circuitry sampled at 1500 Hz by a 16 MHz integrated microcontroller (ATmega328P, Atmel Corporation, San Jose, CA) using a 10-bit successive approximation analog-to-digital converter. Accounting for system gain and differential non-linearity (1 LSB), the system delta value was calculated to be approximately 4 μV. The data read by the microcontroller was streamed to the smartphone via Bluetooth. Calculations were performed and the ECG data was then plotted on the smartphone screen.

To provide a viable human interface, dry electrodes were selected over conventional wet Ag/AgCl electrodes due to their increased durability and lack of a need for skin preparation. 304 grade stainless steel was chosen as the electrode medium due to its high durability and low-cost. Motion-based artifacts are often a concern when employing dry electrodes, however an external input was added to the device to provide the option of choosing an alternative lead input [83].

The system was encased in an Acrylonitrile Butadiene Styrene (ABS) plastic rapid-prototyped case, with recessed locations for the stainless steel differential electrode pair, as well as a reference electrode (Fig. 4.4).

An accompanying application was developed in Android OS to acquire digitized ECG traces and present them to the user on the smartphone screen. A hardware Bluetooth module was used for device communication. Features to save and download traces to an external device were provided in the interface (Fig. 4.4). A beat-to-beat blood flow metric was calculated in each case based on integration of the lead during a single cardiac cycle (Fig. 4.5) [14]. This metric was also displayed on the smartphone interface.

Future Work

In order to verify system accuracy, performance of the device will validated against a commercial 12-lead portable ECG recorder (CardioCard Resting, Nasiff Associates, Central

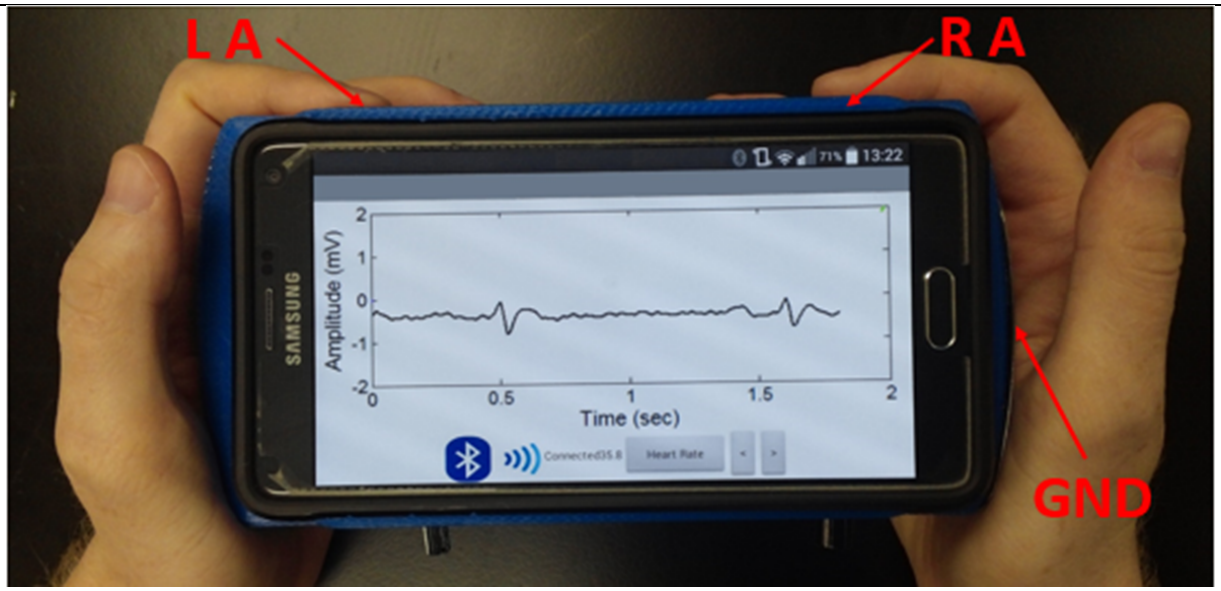

Figure 4.4: System casing and smartphone interface/pairing, illustrating usage in acquiring a conventional ECG trace.

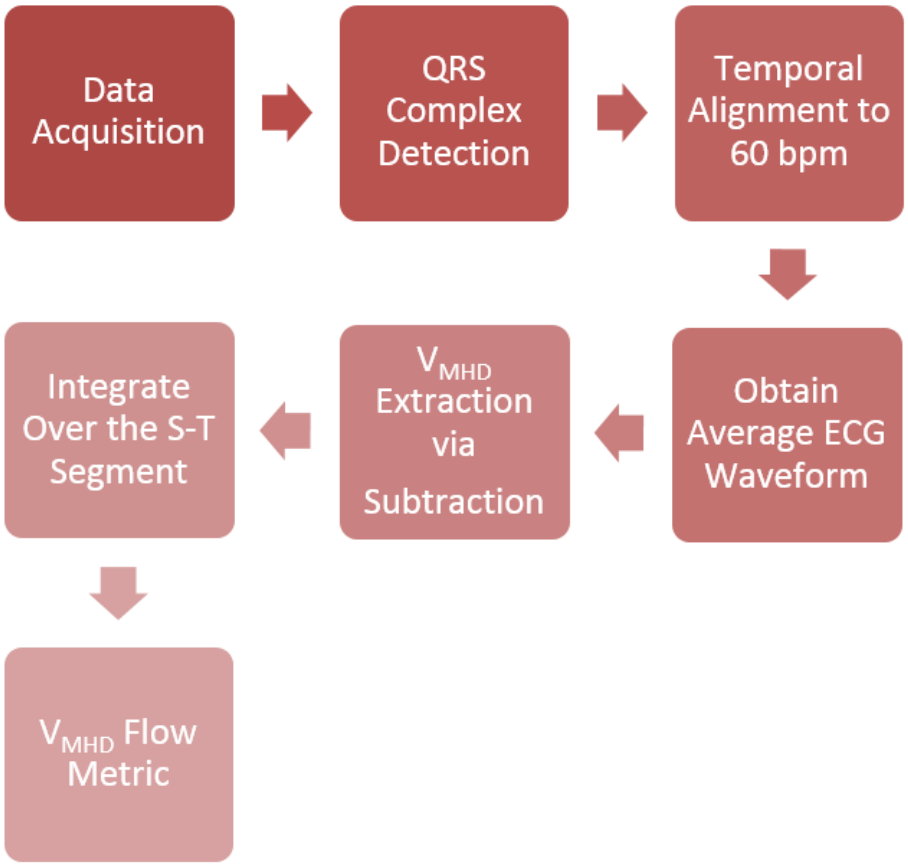

Figure 4.5: Workflow for obtaining V_{MHD} Flow Metrics

Square, NY) set to record single lead ECG traces. Signal deviations in the P-wave, QRS complex, and S-T segment will be calculated for each cardiac cycle and analyzed.

To test the validity of the V_{MHD} metric for blood flow estimation, an experiment should be performed with the device, comparing the measurements of the blood flow metric from the device, with a current gold standard for blood flow measurement (e.g. Doppler Ultrasound). To induce the MHD effect, and generate a voltage overlay on acquired ECG traces, a pair of neodymium magnets will applied to the region of interest ($B_{r,\,max}$ = 0.4T). A custom-fit compression band was used to secure the neodymium magnets to the subject, and maintain proper device positioning with respect to the applied magnetic field. The neodymium magnets were oriented in opposition to create a uniform magnetic field across the measurement volume of the vessel of interest, e.g. brachial (Fig. 4.6). Ultrasound will be used to locate the vessel for positioning of magnets and electrodes.

After validation of the V_{MHD} blood flow metric, studies using the device and paired ultrasound validation with larger populations will also be conducted to better observe the V_{MHD} measured in real world conditions. These continued studies will also allowing for examinations of target groups of the device, including those with peripheral artery disease, and other peripheral vascular issues, which would benefit from longitudinal monitoring. An IRB protocol will be filed with the institutional Human Subjects Office, and will clearly outline the different patient populations that will be recruited for the study (health subjects for baseline measurements, and patient subjects with peripheral artery disease). Before any procedure, subjects would be consented in writing of the procedures and risks of the study, and signed records of consent stored by the principal investigator.

A study to further quantify the relationship between V_{MHD} and electrolytic flow under ideal conditions will be conducted using a flow phantom. The study would vary the strength of the

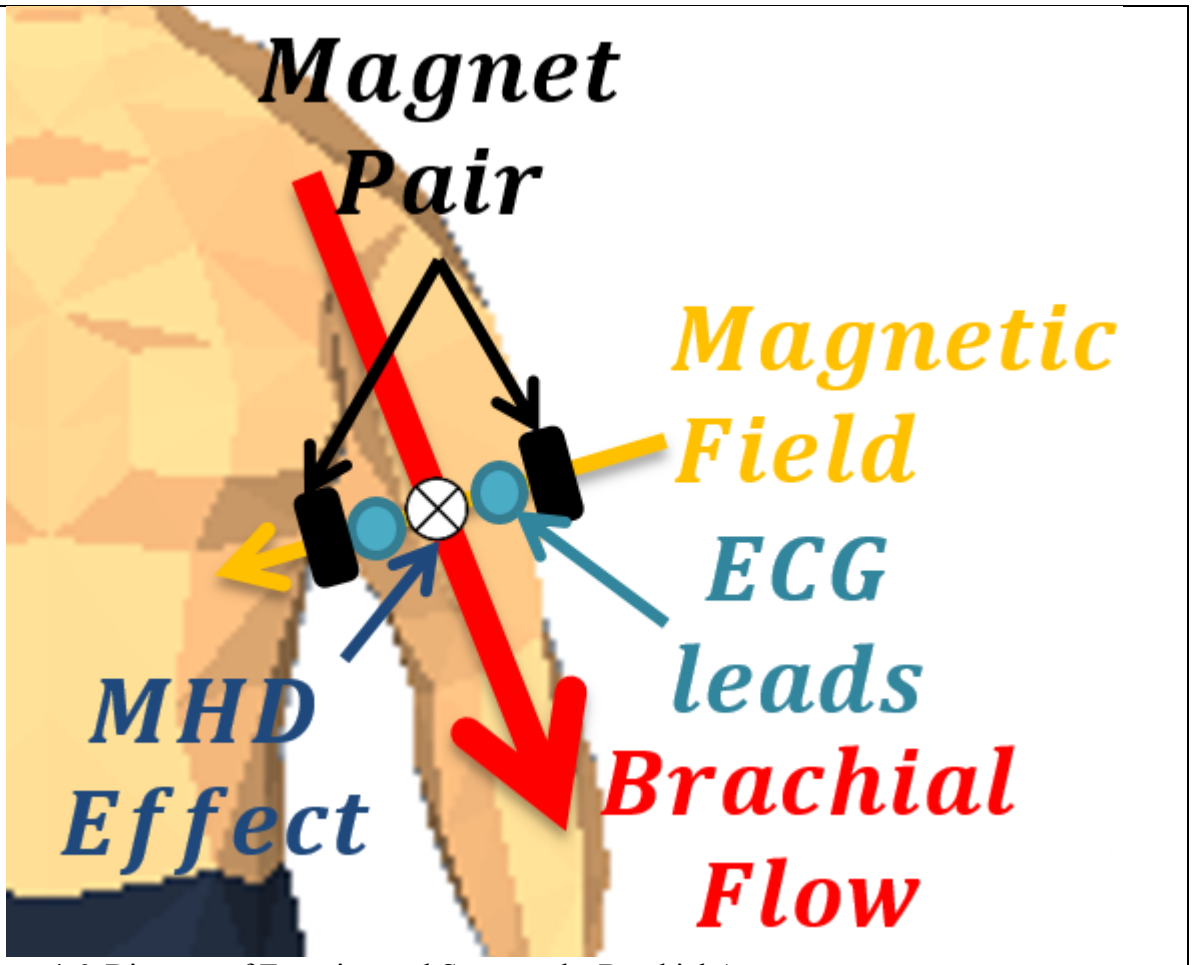

Figure 4.6: Diagram of Experimental Setup at the Brachial Artery

magnetic field to examine the change in the voltage induced to better define the relationship of V_{MHD} under constant flow.

Impact

The V_{MHD} derived blood flow metric offers an alternative method of observing regional blood flow. Currently, the majority of assessment tools require an expensive, immobile device (e.g. MRI scanner, CT scanner, or Ultrasound), cause discomfort for patients, and generally require a skilled technician to operate. Specifically within the MRI scanner, being able to obtain a blood flow measurement via the V_{MHD} induced in vessels allows for more robust physiological monitoring during MR procedures. If the device performs, it would be a low-cost and method for measuring blood flow, allowing the metric to become much more accessible to clinicians as well as the general populace. Like hypertension and diabetes, blood flow is an indicator of cardiovascular health and many experience issues with peripheral circulation. This V_{MHD} based metric and device offer an alternative that can be used to provide many with the longitudinal monitoring needed to keep their conditions in check. In the case of PAD, at risk populations generally only have access to yearly checkups into the status of their peripheral arterial health through the ABI. If the proposed device were used for PAD screening, more conclusive results with the V_{MHD} based flow metric could be offered, rather than just a recommendation that further exams of blood flow need to be ordered. Patients with PAD would also benefit greatly from having a device with which to monitor the progression of their PAD more frequently than on a yearly basis. Furthermore, the presented device provides an advantage over commercially available portable ECG recorders, as it includes additional capabilities in regards to tracking exercise progression and monitoring blood flow.

The integration of smartphone-enabled technology allows for easier data-exporting, data-logging, and sharing with overseeing physicians. As the data is streamed from the device utilizing Bluetooth, any Bluetooth enabled device, not just a smartphone, could be utilized to receive the output of the device, allowing this technology to be adapted by multiple platforms. The creation of this prototype will in turn open doors for many future studies, allowing for better adoption and acceptance of the device, and the upgrade of current features (software and hardware).

Acknowledgements

The initial design for the proposed system was developed by senior design team members Kevin Wu, Sheila Donovan, Augustus Huffines, Bobby Leitmann, Luke Mosteller, and Charles Reeder. This research was supported by a NSF I-Corps Grant (#1617340) and a UGA Clinical and Translational Research Unit Grant.

CHAPTER 5

DEFINING THE RELATIONSHIP OF MAGNETOHYDRODYNAMIC VOLTAGES AND MAGNETIC FIELD STRENGTH[2]

[2] Kevin J, Wu, T.S. Gregory, M.C. Lastinger, B. Boland, Z.T.H. Tse. Accepted by the *Journal of Medical Devices*. Reprinted here with permission of the publisher.

Background

The magnetohydrodynamic (MHD) effect is observed in flowing electrolytic fluids and their interactions with magnetic fields. The magnetic field (B_0), when perpendicular with the electrolytic fluid flow (μ), causes the shift of the charged particles in the fluid to shift across the length of the vessel (L) normal to the plane of B_0 and flow, creating a voltage (V_{MHD}) observable through voltage potential measurements across the flow (Eqn. 5.1)[68].

$$V_{MHD} = \int_0^L (\vec{u} \times \overrightarrow{B_0}) \cdot \overrightarrow{dL} \tag{5.1}$$

In the medical field, this phenomenon is commonly encountered inside of a human body inside of an MRI machine (Fig. 5.1).

The effect appears most prominently inside the aortic arch due to orientation and size; it is a large contributing factor to noise observed in intra-MRI ECGs [1, 2]. Traditionally, this MHD induced voltage (V_{MHD}) was filtered out to obtain clean intra-MRI ECGs, but recent studies have shown that the V_{MHD} induced in a vessel is related to the blood flow through it (stroke volume in the case of the aortic arch) [13]. Further proof of this relationship can be shown from the increase in V_{MHD} measured from periphery blood vessels during periods of elevated heart rate from exercise stress, when compared to baseline state [84]. Previously, a portable device was built to utilize induced V_{MHD} as an indicator of flow. The device was capable of showing change in blood flow, utilizing a blood flow metric obtained from V_{MHD}; however, a quantitative relationship between V_{MHD} and blood flow has yet to be established.

This study aims to define the relationship between induced V_{MHD} and magnetic field strength in a controlled setting. Through modulating the distance between a pair of magnets around a flow channel, we hope to better realize the relationship between magnetic field strength and induced V_{MHD} with constant flow and electrolytic solution concentration.

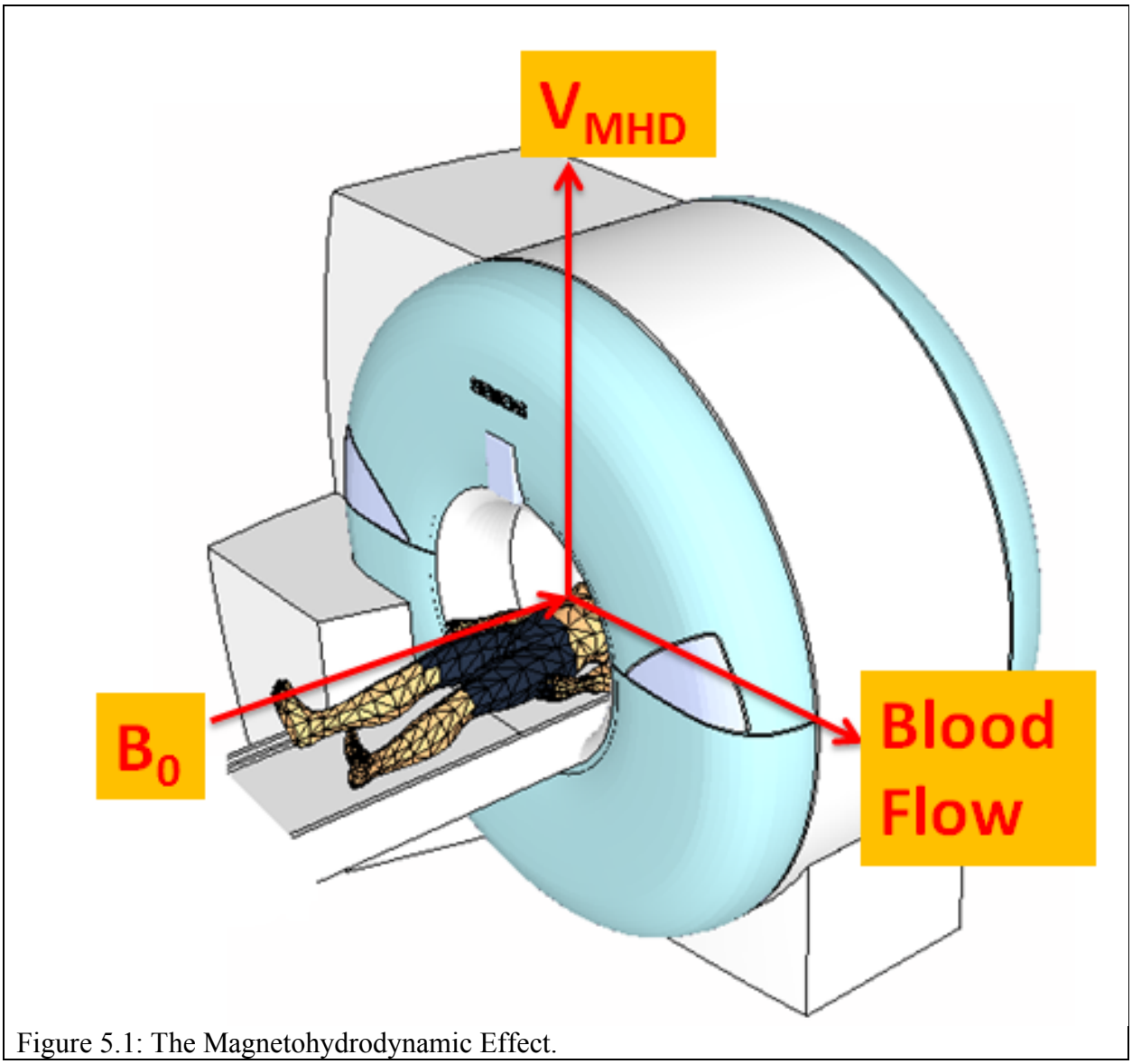

Figure 5.1: The Magnetohydrodynamic Effect.

Methods

There were two main issues to address with the experiment: a benchtop setup that would hold the magnets apart safely at the distances required to generate the desired magnetic field strength while still maintaining the ability to pull the magnets apart, and a data acquisition setup to monitor the minute voltages expected to be induced.

The benchtop setup was fabricated to allow for the safe movement of the magnets towards and away from each other. A pair of cylindrical, N52 grade neodymium magnets of a diameter of 2 inches and a height of 2 inches were used to generate the magnetic field. Utilizing the manufacturer's online calculator for field strength, it was determined that an air gap of 0.5 in. would result in a ~1T field strength. Polyoxymethylene blocks of 6 in by 6 in. by 0.5 in. were machined with 0.25 in. deep sockets to hold the magnets on one face, while 0.75 in. wide slots centered on the other face were machined, allowing for a band of exposed magnet to contact the flow channel for the maximum field strength, while preserving material to form a 0.5 in barrier between the two magnets (Fig. 5.2). The setup was mounted on brackets and then affixed to a vise to allow for safe movement of the two magnets together and apart during the experiment (Fig. 5.3). The actual strength of the magnetic field was verified using a magnetometer, with measurements taking place at the center of the gap between both magnets. It was determined that the minimum field strength of the setup was 0.2T, with a maximum field strength of 0.9T in the air gap between the blocks when the vise was wound closed. The flow channel was designed to be inserted in the slot between the two magnets. A through-channel was designed with barbed ends for the pipe, as well as grooves to insert the measurement wire. The flow channel was fabricated using a sterolithography based 3D printer in order to ensure a watertight model (Fig. 5.4). Coaxial cables

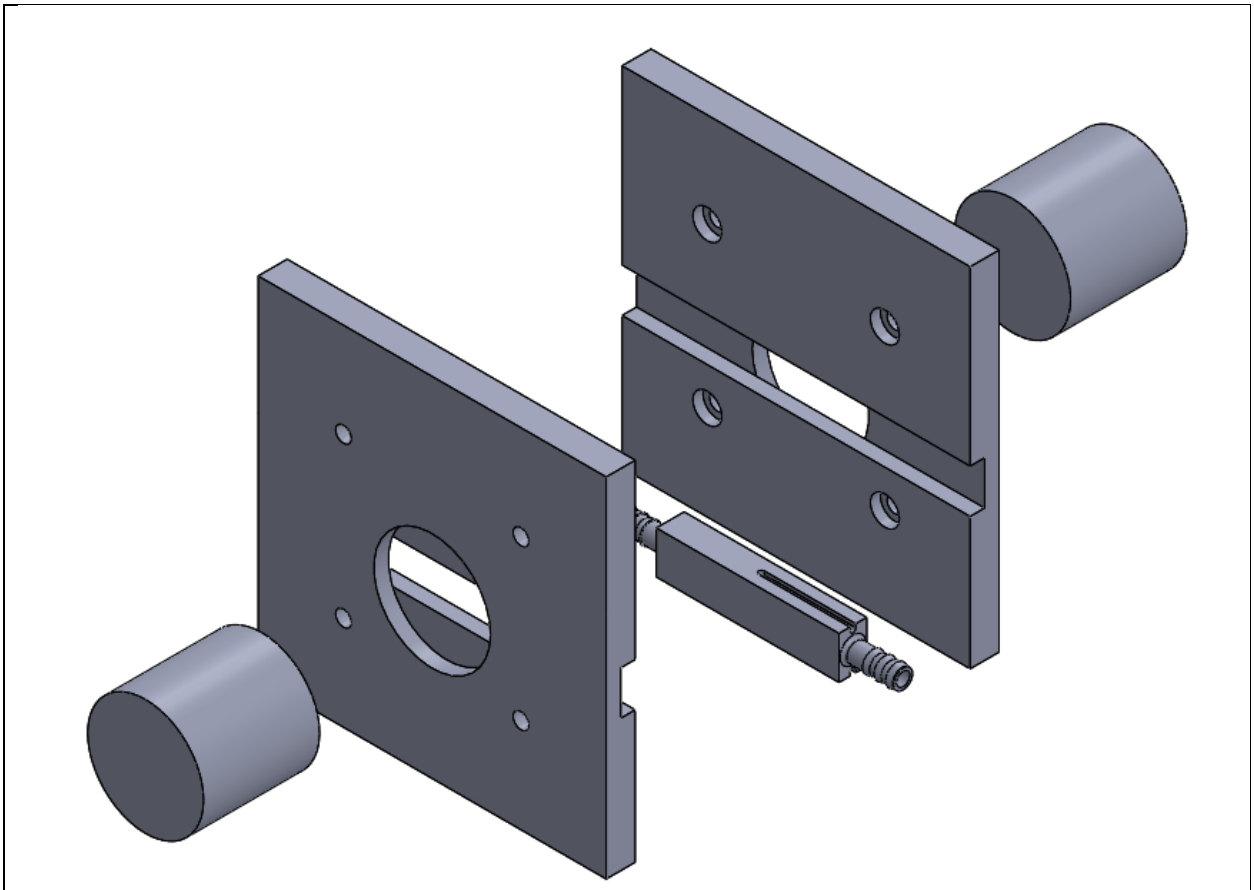

Figure 5.2: Polyoxymethylene Block Design

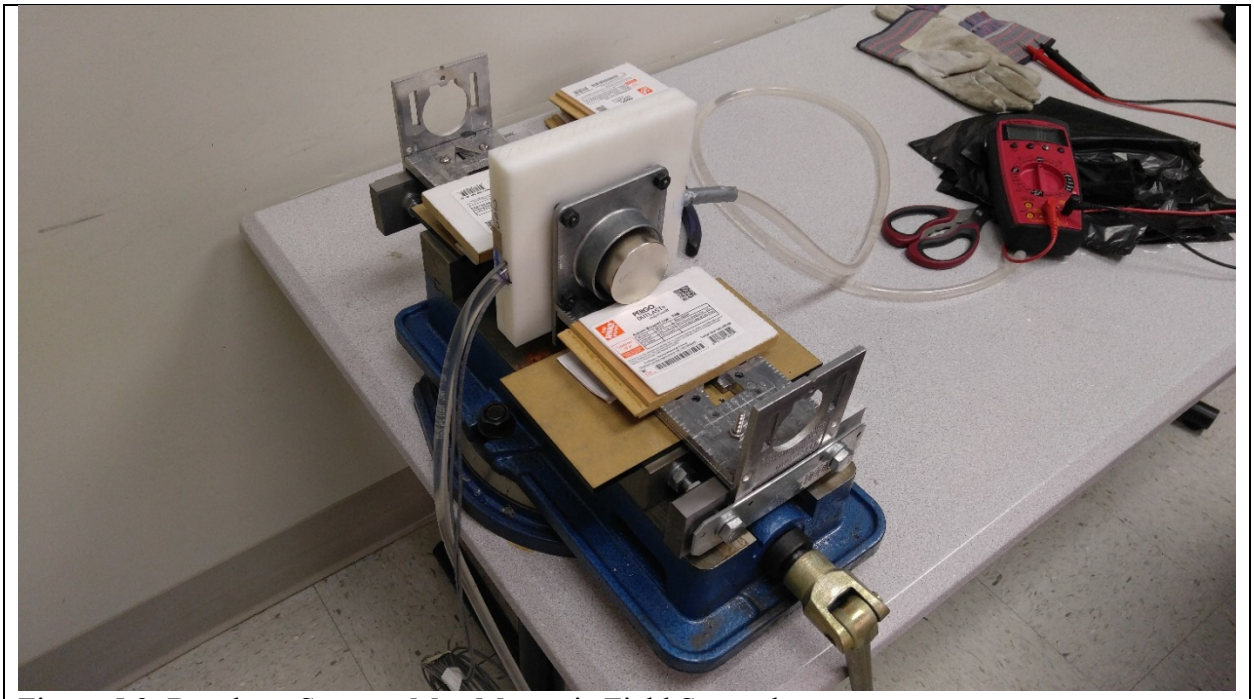

Figure 5.3: Benchtop Setup at Max Magnetic Field Strength

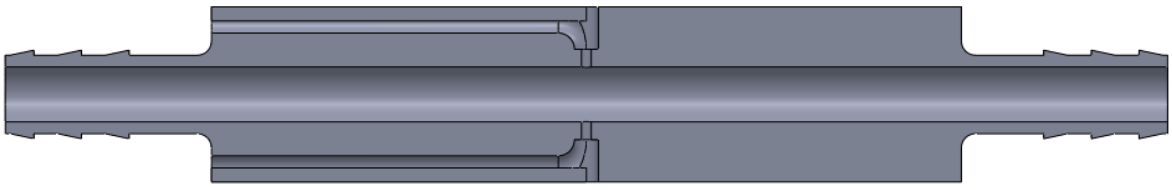

Figure 5.4: Flow Channel Design

were mounted in the flow channels and used to measure the VMHD generated inside the flow channel; the exposed copper wires were used as the electrodes. The electrodes were mounted above and below the flow chamber (normal to the plane of the electrolytic flow and the magnetic field in accordance to the Right Hand Rule) to give a differential measurement.

For the experiment, the flow channel was held in-between the magnets, with the measurement point centered and the voltage measured from the electrodes recorded.

Results

The measured VMHD for the two different flow channels were recorded (Table 5.1). A curve examining the relationship of recorded VMHD¬ vs distance from magnetic field was created (Fig. 5).

Interpretation

The recorded data showed an increase in measured VMHD as the magnetic field increased, which agrees with the theoretical relationship (Eq. 1), as a stronger magnetic field over constant tube diameter and flow velocity would pull more electrolytes and create a greater charge disparity. There was a great increase in the voltage as the magnetic field increased at first, though the VMHD stagnated as the field strength approached 0.9T. This could be, in part, due to the concentration of the electrolytes within the flowing fluid. Theoretically, there would be a maximum voltage that could be induced through the amount of electrolytes present in the flow. In this case, that saturation voltage could have been reached around 0.8 and 0.9T, with the field being strong enough to pull all available electrolytes in the measurement area.

There were a few unexpected drops in voltage particularly in the VMHD measured at 0.5T and 0.6T. This may have occurred through misalignment of the measurement site in between the magnets. Due to the high strength of the magnetic field, some deflection was observed at the two

Table 5.1: Measured VMHD at Different Magnetic Field Strengths

Magnetic Field Strength (T)	V_{MHD} (mV)
0.2	19.5
0.3	26.2
0.4	27.7
0.5	22.8
0.6	26.3
0.7	29.8
0.8	31.4
0.9	31.5

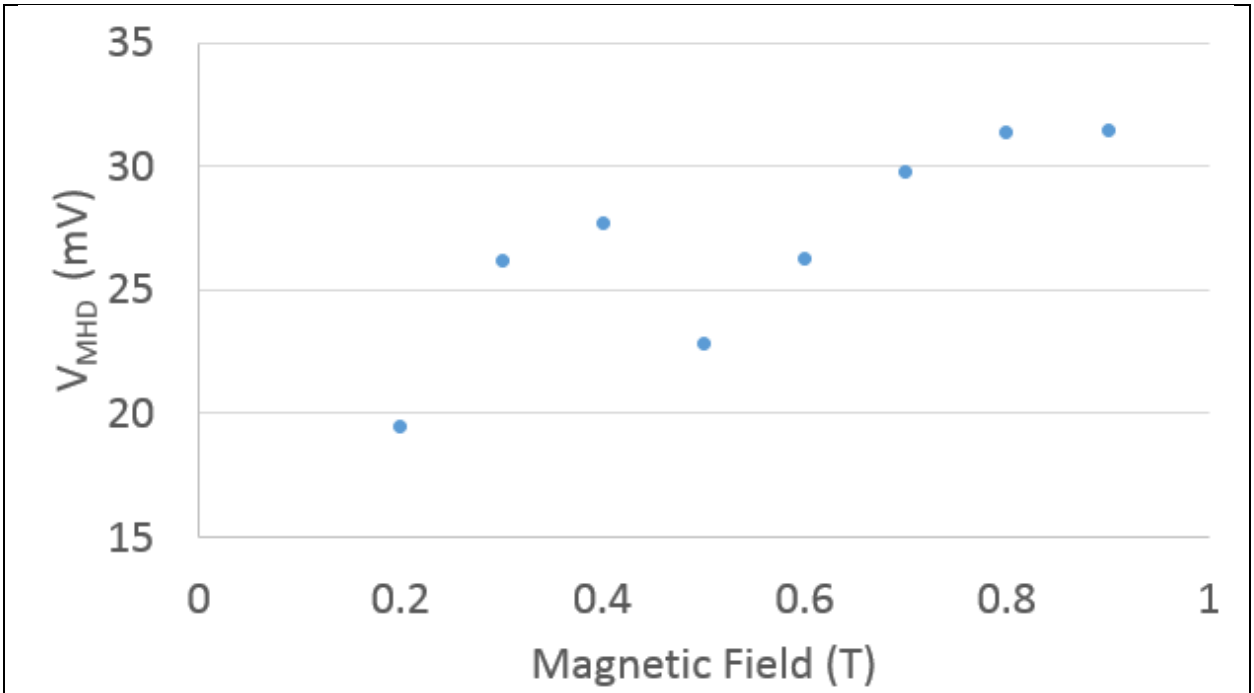

Figure 5.5: Induced V_{MHD} as a Function of Magnetic Field Strength

magnets were brought together, leading to the two polyoxymethylene blocks to “snap” together violently, which was have slightly jostled the positioning of the flow channel and therefore the electrode pair, compared to the measurement area of the sensitive and minute sensor of the magnetometer. For reference, the observed physical distance between the field strength of 0.5T and 0.6T was <1.5mm. However, the general trend of a logarithmic increase of the MHD voltage was still present.

Further applications of the MHD effect would be the development of an alternative method of electrolytic flow measurement. Within the MRI environment, the ability to monitor stroke volume of the heart without needing to use phase contrast imaging would allow for faster procedures and increased physiological monitoring during MR procedures. In addition, magnetohydrodynamic voltages for blood flow measurement can be used in portable applications, which would allow it to function as an alternative method of blood flow monitoring that is both portable and more accessible (due to differences in equipment cost and technical knowledge required for operation) than current standards (Laser Doppler Flowmetry, MRI, and Doppler Ultrasound).

This experiment has provided insight into the relationship between the magnetic field and induced VMHD under controlled conditions. Further studies will focus on the effects of flow rate of the electrolytic fluid and its effects on observed VMHD.

CHAPTER 6

CONCLUSION

The author worked to bring a novel method of flow monitoring through V_{MHD} derived flow metrics from an intra-MRI phenomenon into a real world portable application. First, to better study the induced V_{MHD} from intra-MRI ECGs, an adaptive filtering methodology was created to improve ECG_{Real} extraction from intra-MRI ECGs, while obtaining an isolated source of V_{MHD} from the carotid, which was shown to be correlated to the induced aortic V_{MHD} normally found on intra-MRI ECGs. While nonfunctional in its current state, the main issues hindering with the current methodology have been identified to progress in the project. Next, to improve intra-MRI monitoring capabilities, a paramagnetic choke with a Gadolinium-solution core was developed to decrease observed RF noise on MRI scans when external physiological monitors were use on subjects inside the MRI.

As a proof of concept that V_{MHD} could be reproduced outside of the MRI, a prototype smartphone enabled ECG device was developed that, when used with a pair of magnets, could measure induced voltages in peripheral vessels. In application, the V_{MHD} flow monitor could be used to measure and track flow in peripheral regions, such as in limbs and towards the hands and feet, where current methods of flow measurement are hard pressed to asses regional blood flow. Further work was done with a fabricated benchtop flow phantom setup to begin quantifying how different factors, like electrode placement, magnetic field strength, and flow velocity, could affect V_{MHD} induced in a vessel.

As future work, patient populations should be studied with all the explored technologies within this thesis, especially those presenting with cardiovascular conditions to show the applicability of these technologies under varied conditions, with a protocol in place from the IRB. Further exploration into the different factors affecting the induced V_{MHD} should also be explored to help establish the relationship between the V_{MHD} flow metric and established standard flow units.

REFERENCES

[1] A. Gupta, A. R. Weeks, and S. M. Richie, "Simulation of elevated T-waves of an ECG inside a static magnetic field (MRI)," *IEEE Trans Biomed Eng,* vol. 55, pp. 1890-6, Jul 2008.

[2] Z. Tse, C. L. Dumoulin, G. D. Clifford, J. Schweitzer, L. Qin, J. Oster*, et al.*, "A 1.5T MRI-conditional 12-lead electrocardiogram for MRI and intra-MR intervention," *Magn Reson Med,* vol. 71, pp. 1336-1347, Apr 11 2013.

[3] G. M. Nijm, S. Swiryn, A. C. Larson, and A. V. Sahakian, "Extraction of the magnetohydrodynamic blood flow potential from the surface electrocardiogram in magnetic resonance imaging," *Med Biol Eng Comput,* vol. 46, pp. 729-33, Jul 2008.

[4] S. H. Zhang, T. T. Zion, W. Wang, R. Y. Kwong, C. L. Dumoulin, and E. J. Schmidt, "Computation of the gradient-induced electric field noise in 12-lead ECG traces during rapid MRI sequences," *Journal of Cardiovascular Magnetic Resonance,* vol. 16, p. P151, 2014.

[5] J. Oster, R. Llinares, S. Payne, Z. T. H. Tse, E. J. Schmidt, and G. D. Clifford, "Comparison of three artificial models of the magnetohydrodynamic effect on the electrocardiogram," *Computer methods in biomechanics and biomedical engineering,* pp. 1-18, 2014.

[6] T. S. Gregory, J. Oshinski, E. J. Schmidt, R. Y. Kwong, W. G. Stevenson, and Z. T. Ho Tse, "Continuous Rapid Quantification of Stroke Volume Using Magnetohydrodynamic Voltages in 3T Magnetic Resonance Imaging," *Circ Cardiovasc Imaging,* vol. 8, Dec 2015.

[7] I. BIOPAC Systems, "Signal Processing Methods for use with MRI Artifact Corrupted ECG Waveforms," 03/30/2015.

[8] J. Krug, G. Rose, G. Clifford, and J. Oster, "Improved ECG based gating in ultra high field cardiac MRI using an independent component analysis approach," *Journal of Cardiovascular Magnetic Resonance,* vol. 15, p. 33, 2013.

[9] J. Krug, G. Rose, D. Stucht, G. Clifford, and J. Oster, "Filtering the Magnetohydrodynamic Effect from 12-lead ECG Signals using Independent Component Analysis," *Computing in Cardiology,* pp. 589-592, 2012.

[10] J. Oster, O. Pietquin, R. Abacherli, M. Kraemer, and J. Felblinger, "Independent component analysis-based artefact reduction: application to the electrocardiogram for improved magnetic resonance imaging triggering," *Physiol Meas,* vol. 30, pp. 1381-97, Dec 2009.

[11] Z. T. H. Tse, C. L. Dumoulin, G. D. Clifford, J. Schweitzer, L. Qin, J. Oster*, et al.*, "A 1.5 T MRI-conditional 12-lead electrocardiogram for MRI and intra-MR intervention," *Magnetic Resonance in Medicine,* vol. 71, pp. 1336-1347, 2013.

[12] T. S. Gregory, E. J. Schmidt, S. H. Zhang, and Z. T. H. Tse, "3DQRS: A method to obtain reliable QRS complex detection within high field MRI using 12-lead electrocardiogram traces," *Magnetic Resonance in Medicine,* vol. 71, pp. 1374-1380, 2014.

[13] T. S. Gregory, J. Oshinski, E. J. Schmidt, R. Y. Kwong, W. G. Stevenson, and Z. T. H. Tse, "Continuous Rapid Quantification of Stroke Volume Using Magnetohydrodynamic Voltages in 3T Magnetic Resonance Imaging," *Circulation: Cardiovascular Imaging,* vol. 8, p. e003282, 2015.
[14] H. Elhawary, Z. T. H. Tse, A. Hamed, M. Rea, B. L. Davies, and M. U. Lamperth, "The case for MR-compatible robotics: a review of the state of the art," *The international journal of medical robotics and computer assisted surgery,* vol. 4, pp. 105-113, 2008.
[15] S. Lange and Q. N. NGUYEN, "Cables and electrodes can burn patients during MRI," *Nursing2014,* vol. 36, p. 18, 2006.
[16] E. Atalar and O. Ocali, "Enhanced safety coaxial cables," ed: Google Patents, 2001.
[17] M. E. Ladd and H. H. Quick, "Reduction of resonant RF heating in intravascular catheters using coaxial chokes," *Magnetic resonance in medicine,* vol. 43, pp. 615-619, 2000.
[18] J. DeMarinis, "The antenna cable as a source of error in EMI measurements," in *Electromagnetic Compatibility, 1988. Symposium Record., IEEE 1988 International Symposium on*, 1988, pp. 9-14.
[19] A. Metsler, "Ferrite common mode choke adapted for circuit board mounting," ed: Google Patents, 1996.
[20] Y. Yoshizawa, K. Yamauchi, T. Yamane, and H. Sugihara, "Common mode choke cores using the new Fe-based alloys composed of ultrafine grain structure," *Journal of Applied Physics,* vol. 64, pp. 6047-6049, 1988.
[21] P. A. Bottomley, A. Kumar, W. A. Edelstein, J. M. Allen, and P. V. Karmarkar, "Designing passive MRI-safe implantable conducting leads with electrodes," *Medical physics,* vol. 37, pp. 3828-3843, 2010.
[22] C. M. Hillenbrand, D. R. Elgort, E. Y. Wong, A. Reykowski, F. K. Wacker, J. S. Lewin*, et al.*, "Active device tracking and high-resolution intravascular MRI using a novel catheter-based, opposed-solenoid phased array coil," *Magnetic Resonance in medicine,* vol. 51, pp. 668-675, 2004.
[23] P. Vernickel, C. Findeklee, J. Eichmann, and I. Graesslin, "Active digital decoupling for multi-channel transmit MRI Systems," in *Proceedings of the Joint Annual Meeting of ISMRM-ESMRMB, Berlin, Germany*, 2007, p. 170.
[24] P. A. Bottomley, P. V. Karmarkar, J. M. Allen, and W. A. Edelstein, "Mri and rf compatible leads and related methods of operating and fabricating leads," ed: Google Patents, 2008.
[25] M. Morales, O. Bomati-Miguel, R. P. De Alejo, J. Ruiz-Cabello, S. Veintemillas-Verdaguer, and K. O'Grady, "Contrast agents for MRI based on iron oxide nanoparticles prepared by laser pyrolysis," *Journal of Magnetism and Magnetic Materials,* vol. 266, pp. 102-109, 2003.
[26] J. F. Schenck, "The role of magnetic susceptibility in magnetic resonance imaging: MRI magnetic compatibility of the first and second kinds," *Medical physics,* vol. 23, pp. 815-850, 1996.
[27] K. B. Baker, J. A. Tkach, J. A. Nyenhuis, M. Phillips, F. G. Shellock, J. Gonzalez-Martinez*, et al.*, "Evaluation of specific absorption rate as a dosimeter of MRI-related implant heating," *Journal of Magnetic Resonance Imaging,* vol. 20, pp. 315-320, 2004.
[28] M. F. Dempsey and B. Condon, "Thermal injuries associated with MRI," *Clinical radiology,* vol. 56, pp. 457-465, 2001.

[29] W. R. Nitz, A. Oppelt, W. Renz, C. Manke, M. Lenhart, and J. Link, "On the heating of linear conductive structures as guide wires and catheters in interventional MRI," *Journal of Magnetic Resonance Imaging,* vol. 13, pp. 105-114, 2001.
[30] M. Oudkerk, P. E. Sijens, E. J. VAN BEEK, and T. J. Kuijpers, "Safety and efficacy of dotarem (Gd-DOTA) versus magnevist (Gd-DTPA) in magnetic resonance imaging of the central nervous system," *Investigative radiology,* vol. 30, pp. 75-78, 1995.
[31] J. Pintaske, P. Martirosian, H. Graf, G. Erb, K.-P. Lodemann, C. D. Claussen*, et al.*, "Relaxivity of gadopentetate dimeglumine (Magnevist), gadobutrol (Gadovist), and gadobenate dimeglumine (MultiHance) in human blood plasma at 0.2, 1.5, and 3 Tesla," *Investigative radiology,* vol. 41, pp. 213-221, 2006.
[32] T. A. Franklin, "Ferrofluid flow phenomena," Citeseer, 2003.
[33] A. D. Rosenthal, "Ferrofluid flow and torque measurements in rotating magnetic fields," Massachusetts Institute of Technology, 2002.
[34] S. Foner, "Versatile and sensitive vibrating-sample magnetometer," *Review of Scientific Instruments,* vol. 30, pp. 548-557, 1959.
[35] C. Christodoulides, "Comparison of the Ampere and Biot—Savart magnetostatic force laws in their," *Am. J. Phys,* vol. 56, p. 4, 1988.
[36] P. Pappas, "The original Ampere force and Biot-Savart and Lorentz forces," *Il Nuovo Cimento B (1971-1996),* vol. 76, pp. 189-197, 1983.
[37] M. Gyimesi and D. Ostergaard, "Inductance computation by incremental finite element analysis," *Magnetics, IEEE Transactions on,* vol. 35, pp. 1119-1122, 1999.
[38] T. S. Gregory, E. J. Schmidt, S. H. Zhang, R. Y. Kwong, W. G. Stevenson, J. R. Murrow*, et al.*, "Left-Ventricular Mechanical Activation and Aortic-Arch Orientation Recovered from Magneto-Hydrodynamic Voltages Observed in 12-Lead ECGs Obtained Inside MRIs: A Feasibility Study," *Annals of Biomedical Engineering,* vol. 42, pp. 2480-9, 2014.
[39] ASTM, "Standard Practice for Marking Medical Devices and Other Items for Safety in the Magnetic Resonance Environment," *ASTM International,* vol. F2503, 2005.
[40] ASTM. (2013). *F2119 Standard Test Method for Evaluation of MR Image Artifacts from Passive Implants*. Available: http://www.astm.org/Standards/F2119.htm
[41] K. Katoh and H. Toh, "Recent developments in the MAFFT multiple sequence alignment program," *Briefings in bioinformatics,* vol. 9, pp. 286-298, 2008.
[42] D. M. West and E. A. Miller, *Digital medicine: Health care in the Internet era*: Brookings Institution Press Washington, DC, 2009.
[43] R. Fensli, E. Gunnarson, and O. Hejlesen, "A wireless ECG system for continuous event recording and communication to a clinical alarm station," in *Engineering in Medicine and Biology Society, 2004. IEMBS'04. 26th Annual International Conference of the IEEE*, 2004, pp. 2208-2211.
[44] W. H. Righter, "Portable ECG monitor/recorder," ed: Google Patents, 1993.
[45] W. H. Righter, A. J. Nicoll, and H. L. Kennedy, "Portable, multi-channel ECG data monitor/recorder," ed: Google Patents, 1994.
[46] J. J. Segura-Juárez, D. Cuesta-Frau, L. Samblas-Pena, and M. Aboy, "A microcontroller-based portable electrocardiograph recorder," *IEEE transactions on biomedical engineering,* vol. 51, pp. 1686-1690, 2004.

[47] M. Shojaei-Baghini, R. K. Lai, and D. K. Sharma, "A low-power and compact analog CMOS processing chip for portable ECG recorders," in *Asian Solid-State Circuits Conference, 2005*, 2005, pp. 473-476.
[48] K. T. Hickey, J. Dizon, and A. Frulla, "Detection of Recurrent Atrial Fibrillation Utilizing Novel Technology," *JAFIB: Journal of Atrial Fibrillation,* vol. 6, 2013.
[49] E. H. Chung and K. D. Guise, "QTC intervals can be assessed with the AliveCor heart monitor in patients on dofetilide for atrial fibrillation," *Journal of electrocardiology,* vol. 48, pp. 8-9, 2015.
[50] D. Albert, B. R. Satchwell, and K. N. Barnett, "Wireless, ultrasonic personal health monitoring system," ed: Google Patents, 2012.
[51] B. Dolan, "AliveCor launches smartphone-enabled heart monitor, analysis services direct-to-consumer," ed: MobiHealth-News, 2014.
[52] V. Martin, A. Drochon, O. Fokapu, and J.-F. Gerbeau, "MagnetoHemoDynamics in the Aorta and Electrocardiograms," *Phys Med Biol,* vol. 57, pp. 3177-3195, 2012.
[53] T. S. Gregory, E. J. Schmidt, S. H. Zhang, R. Y. Kwong, W. G. Stevenson, J. Oshinski*, et al.*, "Rapid Quantification of Stroke Volume using Magnetohydrodynamic Voltages in 3T MRI: A Feasibility Study," *Journal of Cardiovascular Magnetic Resonance,* 2015.
[54] A. Kyriakou, E. Neufeld, D. Szczerba, W. Kainz, R. Luechinger, S. Kozerke*, et al.*, "Patient-specific simulations and measurements of the magneto-hemodynamic effect in human primary vessels," *Physiol Meas,* vol. 33, pp. 117-30, Feb 2012.
[55] D. Mozaffarian, E. J. Benjamin, A. S. Go, D. K. Arnett, M. J. Blaha, M. Cushman*, et al.*, "Heart Disease and Stroke Statistics—2016 Update," *A Report From the American Heart Association,* vol. 133, pp. e38-e360, 2016-01-26 00:00:00 2016.
[56] A. H. Association, *Heart and stroke facts*: The Association, 1993.
[57] M. Di Carli, J. Czernin, C. K. Hoh, V. H. Gerbaudo, R. C. Brunken, S.-C. Huang*, et al.*, "Relation among stenosis severity, myocardial blood flow, and flow reserve in patients with coronary artery disease," *Circulation,* vol. 91, pp. 1944-1951, 1995.
[58] T. Heitzer, T. Schlinzig, K. Krohn, T. Meinertz, and T. Münzel, "Endothelial dysfunction, oxidative stress, and risk of cardiovascular events in patients with coronary artery disease," *Circulation,* vol. 104, pp. 2673-2678, 2001.
[59] D. N. Ku, "Blood flow in arteries," *Annual Review of Fluid Mechanics,* vol. 29, pp. 399-434, 1997.
[60] J. R. Sowers, M. Epstein, and E. D. Frohlich, "Diabetes, hypertension, and cardiovascular disease an update," *Hypertension,* vol. 37, pp. 1053-1059, 2001.
[61] A. M. Weissler, R. G. Peeler, and W. H. Roehll Jr, "Relationships between left ventricular ejection time, stroke volume, and heart rate in normal individuals and patients with cardiovascular disease," *American heart journal,* vol. 62, pp. 367-378, 1961.
[62] M. S. Rendell, B. K. Milliken, M. F. Finnegan, D. A. Finney, and J. C. Healy, "The skin blood flow response in wound healing," *Microvascular research,* vol. 53, pp. 222-234, 1997.
[63] N. I. o. Health. (2016, May 3). *How Is Peripheral Artery Disease Diagnosed?* Available: https://www.nhlbi.nih.gov/health/health-topics/topics/pad/diagnosis
[64] T. Gregory, E. Schmidt, S. Zhang, and Z. Tse, "3DQRS: A method to obtain reliable QRS complex detection within high field MRIs using 12-lead ECG traces.," *Magnetic Resonance in Medicine,* vol. 71, pp. 1374-1380, 2014.

[65] T. Togawa, O. Okai, and M. Oshima, "Observation of blood flow EMF in externally applied strong magnetic field by surface electrodes," *Medical and Biological Engineering and Computing,* vol. 5, pp. 169-170, 1967.
[66] D. Abi-Abdallah, V. Robin, A. Drochon, and O. Fokapu, "Alterations in human ECG due to the MagnetoHydroDynamic effect: a method for accurate R peak detection in the presence of high MHD artifacts," *Conf Proc IEEE Eng Med Biol Soc,* pp. 1842-5, 2007.
[67] T. Birkholz, M. Schmid, C. Nimsky, J. Schuttler, and B. Schmitz, "ECG artifacts during intraoperative high-field MRI scanning," *J Neurosurg Anesthesiol,* vol. 16, pp. 271-6, Oct 2004.
[68] G. Nijm, S. Swiryn, A. Larson, and A. Sahakian, "Extraction of the magnetohydrodynamic blood flow potential from the surface electrocardiogram in magnetic resonance imaging," *Med Biol Eng Comput,* vol. 46, pp. 729-733, 2008.
[69] S. E. Fischer, S. A. Wickline, and C. H. Lorenz, "Novel real-time R-wave detection algorithm based on the vectorcardiogram for accurate gated magnetic resonance acquisitions," *Magn Reson Med,* vol. 42, pp. 361-70, Aug 1999.
[70] M. Hazas and A. Hopper, "Broadband ultrasonic location systems for improved indoor positioning," *Mobile Computing, IEEE Transactions on,* vol. 5, pp. 536-547, 2006.
[71] E. Agu, P. Pedersen, D. Strong, B. Tulu, Q. He, L. Wang*, et al.*, "The smartphone as a medical device: Assessing enablers, benefits and challenges," in *Internet-of-Things Networking and Control (IoT-NC), 2013 IEEE International Workshop of*, 2013, pp. 48-52.
[72] A. Aldaoud, C. Laurenson, F. Rivet, M. R. Yuce, J. M. Redout, and x00E, "Design of a Miniaturized Wireless Blood Pressure Sensing Interface Using Capacitive Coupling," *IEEE/ASME Transactions on Mechatronics,* vol. 20, pp. 487-491, 2015.
[73] K. Mercer, L. Giangregorio, E. Schneider, P. Chilana, M. Li, and K. Grindrod, "Acceptance of Commercially Available Wearable Activity Trackers Among Adults Aged Over 50 and With Chronic Illness: A Mixed-Methods Evaluation," *JMIR mHealth uHealth,* vol. 4, p. e7, 2016.
[74] K. Y. Yazdandoost and R. Kohno, "Wireless Communications for Body Implanted Medical Device," in *Microwave Conference, 2007. APMC 2007. Asia-Pacific*, 2007, pp. 1-4.
[75] D. Panescu, "Emerging Technologies [wireless communication systems for implantable medical devices]," *IEEE Engineering in Medicine and Biology Magazine,* vol. 27, pp. 96-101, 2008.
[76] S. H. Kim, C. H. Yu, and K. Ishiyama, "Rotary-Type Electromagnetic Power Generator Using a Cardiovascular System As a Power Source for Medical Implants," *IEEE/ASME Transactions on Mechatronics,* vol. 21, pp. 122-129, 2016.
[77] P. Kligfield, L. S. Gettes, J. J. Bailey, R. Childers, B. J. Deal, E. W. Hancock*, et al.*, "Recommendations for the standardization and interpretation of the electrocardiogram: part I: the electrocardiogram and its technology a scientific statement from the American Heart Association Electrocardiography and Arrhythmias Committee, Council on Clinical Cardiology; the American College of Cardiology Foundation; and the Heart Rhythm Society endorsed by the International Society for Computerized Electrocardiology," *Journal of the American College of Cardiology,* vol. 49, pp. 1109-1127, 2007.

[78] P. Kligfield and P. M. Okin, "Prevalence and clinical implications of improper filter settings in routine electrocardiography," *The American journal of cardiology,* vol. 99, pp. 711-713, 2007.
[79] A. S. Berson and H. V. Pipberger, "Electrocardiographic distortions caused by inadequate high-frequency response of direct-writing electrocardiographs," *American heart journal,* vol. 74, pp. 208-218, 1967.
[80] C. Zywietz, G. Wagner, and B. Scherlag, "Sampling rate of ECGs in relation to measurement accuracy," *Computerized Interpretation of the Electrocardiogram. New York, NY: Engineering Foundation,* pp. 122-5, 1986.
[81] F. Bessette and L. Nguyen, "Automated electrocardiogram analysis: the state of the art," *Informatics for Health and Social Care,* vol. 14, pp. 43-51, 1989.
[82] S. Jalaleddine, C. G. Hutchens, R. D. Strattan, and W. Coberly, "ECG data compression techniques-a unified approach," *Biomedical Engineering, IEEE Transactions on,* vol. 37, pp. 329-343, 1990.
[83] B. A. Taheri, R. T. Knight, and R. L. Smith, "A dry electrode for EEG recording," *Electroencephalography and clinical neurophysiology,* vol. 90, pp. 376-383, 1994.
[84] T. S. Gregory, E. J. Schmidt, S. H. Zhang, R. Y. Kwong, W. G. Stevenson, J. Oshinski*, et al.*, "Rapid quantification of stroke volume using magnetohydrodynamic voltages in 3T MRI: a feasibility study," *Journal of Cardiovascular Magnetic Resonance,* vol. 17, p. P32, 2015.

APPENDIX A

LIST OF PUBLICATIONS

Journal Publications:

K. J. Wu, T. S. Gregory, J. Oshinski, Z. T. H. Tse, "Intra-MRI Extraction of Diagnostic Electrocardiograms Using Carotidal Magnetohydrodynamic Voltages," Preparing for Submission.

K. J. Wu, T. S. Gregory, W. Zhao, R. Cheng, L. Mao, E. Schmidt, Z. T. H. Tse, "Magnetic Resonance Conditional Paramagnetic Choke for Suppression of Electromagnetic Interference in Electrophysiological Conducting Leads," IMechE, Part H: Journal of Engineering in Medicine, Submitted, 2017

K. J. Wu, T. S. Gregory, J. Moore, B. Hooper, D. Lewis, and Z. T. H. Tse, "Development of an Indoor Guidance System for Unmanned Aerial Vehicles with Power Industry Applications," IET Radar, Sonar, and Navigation, ISSN 1751-8792, 2016.

T. S. Gregory, **K. J. Wu**, J. Yu, J. B. Box, R. Cheng, L. Mao, et al., "Magnetohydrodynamic-Driven Design of Microscopic Endocapsules in MRI," IEEE/ASME Trans. Mechatronics, vol. 20, pp. 2691-2698, 2015.

Selected Conference Publications

K. J. Wu, T. S. Gregory, M. C. Lastinger, B. Boland, Z. T. H. Tse, “Defining the Relationship of Magnetohydrodynamic Voltages and Magnetic Field Strength,” Accepted, Design of Medical Devices 2017

M. DaSilva, **K. J. Wu**, T. S. Gregory, J. R. Murrow, Z. T. H. Tse, “Hemodynamic Quantification with Magnetohydrodynamic Voltages through a Flow Phantom,” Biomedical Engineering Society Annual Meeting, 2016

T. S. Gregory, **K. J. Wu**, E. J. Schmidt, J. Oshinski, and Z. T. H. Tse, "Intra-MRI Extraction of Diagnostic Electrocardiograms using Dynamic Feedback from Carotidal Magnetohydrodynamic Voltages " Journal of Cardiovascular Magnetic Resonance, vol. 18, 2016.

K. J. Wu, T. S. Gregory, E. J. Schmidt, J. Oshinski, Z. T. H. Tse, “Comparison of Carotidal and Aortic Flow as an Indicator of Magnetohydrodynamic Voltages Overlaid on Electrocardiograms in 3T MRI,” 11th Interventional MRI (IMRI) Symposium, Baltimore, MD, USA, 2016

T. S. Gregory, **K. J. Wu**, J. Yu, J. B. Box, R. C. Cheng, L. Mao, et al., "Magnetohydrodynamically Design of Radiofrequency Powered Microscopic Endocapsules in 3T MRI," Proceedings of the 20th Annual Scientific Meeting of the International Society for Magnetic Resonance in Medicine, Toronto, ON, Canada, 2015.